Chapter 7

Giant second harmonic generation in two-dimensional Tellurene engineered by plasma assisted thinning process

Current nonlinear optical (NLO) devices typically rely on conventional non-linear optical materials, which are normally bulk crystals like lithium niobate ($LiNbO_3$). However, as the demand for miniaturization continues to rise, there are significant challenges associated with integrating these traditional NLO materials into other material platforms suitable for on-chip applications. These challenges arise due to technical limitations related to fabrication and integration technologies. Emergence of TMD materials and their attractive physical features holds the key to addressing the upcoming challenges in nano photonics, but their intrinsic second order susceptibilities prevent the direct usage as the NLO crystal. For example, in the previous Chapters 4 and 5, the utilization of biaxial strain and dome structure is introduced to enhance the SHG performance of monolayer TMDs, aiming to enhance their potential for future applications.

In this context, the discovery of new materials with substantial NLO responses and feasibility to integrate onto chips becomes important for the future of photonics and

optoelectronics. Tellurium is a chemical element denoted by the symbol Te and atomic number 52, in the same group as Sulfur and Selenium in the periodic table. This material is believed to have a giant second nonlinear optical susceptibility, even comparable to the conventional nonlinear optical crystal $LiNbO_3$. Remarkably, the crystalline structure of tellurium comprises parallel helical chains of Te atoms, facilitating its feasible transformation into a 2D form known as Tellurene. However, unlike other 2D materials like TMDs, the fabrication of Tellurene through mechanical exfoliation is challenging due to the presence of strong vdW interlayer forces. This chapter thus will investigate 2D Tellurium, and its robust second order nonlinear optical response. A face-to-face stacked substrate configuration is employed in the PVD growth process. This configuration creates a confined zone, thus providing a local growth environment to facilitate the yield of ultra-thin Te flakes. Comprehensive SHG tests on these Te flakes experimentally affirm the outstanding SHG response, though it is limited by sample thickness. To engineer the thickness of the Te flake after the growth process, the interplay between Te and H^+ was capitalised. Hydrogen plasma has been applied to controllably remove the excess portion, thereby achieving the desired thickness for optimal SHG behaviour.

This work not only presents a feasible concept for fabricating ultra-thin high quality Te flakes, and but also introduces a universal method to modulate the thickness of Te samples produced by other methods. At the same time, using etching gas as the post-growth process also offers valuable ideas to precisely process other tellurium samples for potential applications. For instance, Te, with its semiconducting properties, could potentially replace silicon in the construction of novel integrated chips at the nanoscale.

Giant Second Harmonic Generation in Two-Dimensional Tellurene Engineered by Plasma Assisted Thinning Process.

Boqing Liu[†], Kun Liang[†], Qingyi Zhou[‡], Zhuoyuan Lu[†], Ahmed Raza Khan[†], Tanju Yildirim[§], Xueqian Sun[†], Sharidya Rahman[†], Yun Liu[‖], Zongfu Yu[‡], Yuerui Lu*[, †, ※]

[†] School of Engineering, College of Engineering, Computing & Cybernetics, The Australian National University, Canberra, ACT 2601, Australia

[‡] Department of Electrical and Computer Engineering, University of Wisconsin, WI, Madison, 53706, USA

[§] Center for Functional Sensor & Actuator (CFSN), Research Center for Functional Materials, National Institute for Materials Science (NIMS), 1-1 Namiki, Tsukuba, Ibaraki 305-0044, Japan

[‖] Research School of Chemistry, College of Science, The Australian National University, Canberra, ACT 2601, Australia

[※] ARC Centre of Excellence in Quantum Computation and Communication Technology ANU node, Canberra, ACT 2601, Australia

*To whom correspondence should be addressed: Yuerui Lu (yuerui.lu@anu.edu.au)

Chapter 7 Giant second harmonic generation in two-dimensional Tellurene engineered by plasma assisted thinning process

Abstract

Second harmonic generation (SHG) is a prominent branch of non-linear optics (NLO) which heavily relies upon conventional bulk NLO crystals. However, difficulty in downsizing conventional NLO crystals imposes technical limitations towards the future of miniaturized NLO devices. A promising candidate to overcome these restrictions is tellurene, which excels in electrical applications and is considered to possess giant second order optical susceptibility comparable to those of conventional NLO crystals. Herein, face-to-face stacked substrates is employed for the synthesis of tellurene *via* PVD under vacuum conditions. The SHG behavior of tellurene outperforms the transition metal dichalcogenides monolayers by two orders of magnitude, with the maximum efficiency when the flake thickness is between 16-20 nm. To manipulate tellurene thickness, engineered hydrogen plasma etching functions as a post-growth thinning process to successfully control the flake thickness, for optimal SHG, establishing a foundation for controlled tellurene thickness and broadening its potential in diverse applications.

Introduction

Since the discovery of graphene, intensive investigations into two-dimensional (2D) group III and V single-element transition metals, including borophene[1], silicene[2], germanene[3], phosphorene[4] and antimonene[5], have gained significant momentum, due to their promising semi-metallic and semiconducting properties[6]. In 2017, 2D Tellurium known as tellurene with a crystal structure consisting of atomic helical chains that spiral along one of the axes of the crystal lattice was successfully fabricated[7,8]. Bulk phase tellurium (Te) possesses intriguing properties including semiconducting capabilities[9,10], photoconductivity[11], thermoelectricity[12], and piezoelectricity[13], which are widely used in in electronics, sensors, optoelectronics, and energy devices. At the same time, it also possesses comparable capability for non-linear optical properties to conventional crystals, such as $LiNbO_3$, owing to its giant second order susceptibility[14,15]. Tellurene not only well preserves these merits in its two dimensional form[16], but also exhibits extraordinary carrier mobility[17], environmental stability[18] and low thermal conductivity[19], when compared to other 2D materials, such as transition metal dichalcogenides (TMDCs) and black phosphorus (BP)[6,20]. Tellurene's intrinsic nanoscale properties demonstrate potential for high-performance nano- and micro-devices, including field-effect transistors[21], Peltier coolers[22], and quantum hall effect devices[23]. Moreover, tellurene's versatile optical properties signify its potential as an outstanding candidate in future optical devices. For example, the exceptional light absorption of tellurene in the mid-infrared and infrared range offers a platform for the development of future photonics, such as photodetectors[24-26]. Meanwhile, given the wideband nonlinear saturation absorption and strong light-matter interaction from visible to infrared range, nonlinear

photonic devices based on tellurene can function as a **saturable absorber**[27], photonic diode and all-optical switcher[28].

Second harmonic generation (SHG) is an important branch of nonlinear optics, which arises in materials with broken inversion symmetry under an intense optical pump, and plays an important role in the application of imaging and frequency conversion[29]. However, even though the unique helical chain structure of tellurene has been proven to have robust spontaneous polarization and exhibits a giant second order coefficient $\chi^{(2)}$ [14,30], there is lack of comprehensive investigation and work confirming the presence of its extraordinary SHG. This could be attributable primarily to the fact that strong SHG was not observed in tellurene flakes produced in previous reports due to the tellurene fabrication methods used. Specifically, the solution apporach generally is an effective way to produce thin layers, but the synthesis process introduces defects and contaiminants, lowering the purity and crystallinity[31]. On the other hand, vapor deposition methods can ensure the samples' purity and quality, but the samples are quite thick[25,32]. Possible defects in the crystal strucutre and optical interference effects may induce thickness variations, which inevitably confines SHG emission efficiency of thin tellurene flakes, leading to an underestimation of the potential of tellurene as a promising crystal for second order non-linear optics.

In this work, we observed extraordinary SHG performance from tellurene flakes fabricated via confined zone physical vapor deposition (PVD). This method effectively promotes a higher yield of high-quality tellurene flakes with a 30 nm thickness reduction compared to other vapor deposition methods. Comprehensive SHG measurements reveal that the intensity of tellurene flakes easily surpass TMD monolayer films, by up to two

orders of magnitude. Furthermore, the emission efficiency is highly sensitive to the flake thickness and excitation wavelength, where 16 to 20 nm thick flakes demonstrate optimal performance within the wavelength range of 830 nm to 1040 nm. Owing to the reliable reaction between Te and hydrogen ions (H^+), hydrogen plasma etching was adopted as the post growth thinning process to realize modulation of the sample thickness. The well-preserved crystallinity of the processed tellurene samples ensures giant SHG emission, offering a promising approach to improve the application value of tellurene in future nonlinear photonic devices.

Results and discussion

Preparation and characterization of low-dimensional Te

PVD is widely unutilized to synthesize high-quality single crystal films. Compared to traditional PVD methods for tellurene production, this work uses a face-to-face contact stacked substrate configuration and ultra-high vacuum condition to successfully produce tellurene flakes (Figure 1a). The high purity Te precursor and stacked substrates are placed in the heating zone and growth zone near the insulation region prior to the growth procedure. An appropriately set distance between the heating and growth zones, coupled with proper pumping down procedures, synergistically contributes to the efficient deposition temperature for producing thin 2D flakes (see methods). With an increase in temperature, and the application of a vacuum, the solid Te precursor vaporizes and converts into Te molecules, which then can transfer into the narrow space between substrates, finally depositing onto the bottom substrate (Figure 1b). During this process, appropriate temperature and time empower Te molecules to overcome the formation energy barrier, enabling lateral movement for the van der Waals epitaxy[33]. Consequently, Te forms covalent bonds in a helical chain configuration,

primarily aligned along the $[000\bar{1}]$ direction, where this initial bonding arrangement triggers the growth of Te nanowires (1D), followed by the epitaxial growth in lateral and vertical directions, manifesting in the formation of tellurene flakes (Figures 1b and c). Stacking substrates appears to provide a confined-growth space configuration, remarkably stabilizing the flow rate between substrates, which establishes a controllable growth environment for yielding thin flakes[34-36]. While pumping down, the gas flow velocity outside of the confined space is further increased to effectively lower deposition and crystallization temperature, which is crucial for tellurene's morphological evolution[25,31,37]. Hence, the vacuum conditions and the arrangement of stacked substrates play vital roles in modulating the relevant growth energies and kinetics, contributing favorably to the formation, yield, and uniformity of thin tellurene flakes (Figure 1d). Taking advantage of this method, we find that more than half of the tellurene flakes are thinner than 35 nm, and around 31% of the could be as thin as 25 nm (Figure 1e), which is significantly larger yield compared to single crystal thin flakes (<50nm) fabricated by other vapor deposition methods[25,31,33,37], and is comparable to the products of solution synthesis methods[21]. Raman tests, encompassing investigations into thickness, angle, and temperature dependencies were conducted (SI note 1 and Fig S1-3), which strongly reaffirm the high purity and crystalline quality of the synthesized tellurene, consistent with earlier findings in the literature[19,21,25,38].

Nonlinear optical properties of as synthesized tellurene nanoflakes

Tellurene is believed to possess great potential for SHG, doubling frequency of excitation light, owing to its helical chain structure and non-centrosymmetric crystal structure (Figure 2a)[14,39]. To confirm SHG properties, a tellurene flake was examined

with a laser source at a wavelength of 900 nm in response to varying excitation powers. The results demonstrate that the emission intensity became stronger as the excitation power increased, which is described by a linear relationship with a fitting slope value approximately equal to 2.01 (Figure 2b). This indicated that the emission intensity is proportional to the square of the power of the laser beam, complying with the SHG principle[39-43], further elucidating the SH emission of tellurene. A quick comparison between the tellurene flake and monolayer TMD materials under the same excitation setting (Figure 2c) reveal that the tellurene exhibits an enormous SHG signal, surpassing the signal strength of various monolayer TMD flakes by a factor of at least 60. Such extraordinary performance arises due to the high second order nonlinear susceptibility induced by the unique electronic structure and related dipole transition of Te[14]. In addition, the nonlinear anisotropic response was also investigated using a polarization dependent experimental setup for angled SHG response of the tellurene flake. When the sample was rotated and the orientation of the Te helical chain was perpendicular and parallel to the polarized incident light, a maximum and minimum SHG response was obtained, as depicted in the polar plot (Figure 2d). The double petal pattern of SHG demonstrates the SHG emission is sensitive to the azimuthal angle of the tellurene sample, whereas the slender shape of the petals validated the lattice structure's outstanding anisotropic nonlinear optical properties. This observation is consistent with previous findings[30,39]. The experimental intensity data can be well fitted by

$$I = I_0 \cos^2(\theta) \tag{2}$$

where I_0 is the maximum SHG intensity, and θ is the angle between the polarization of incident light and the rotated sample orientation.

Flake thickness also substantially influences the SHG emission as demonstrated in Figure 2d, which depicts the extracted SHG intensity from thicker tellurene flakes spanning a thickness range from 4 to 90 nm, all measured at a wavelength of 900 nm. When the sample thickness is between 17nm to approximately 30nm, there is a distinct decrease in SHG, followed by an increase and decline in SHG intensities associated with the thicker flakes (Figure 2e). This variation is also observed in the tapered-face sample, where robust emission is apparent across regions with a thickness of less than 20 nm, and the strongest local emission is centered around a thickness of 17 nm (Figure S4). This behavior is well explained by the phase matching originating from the interference of the fundamental and SHG waves within the flake and SiO_2 layer (275 nm), which serves as a Fabry–Perot cavity[40,44]. The finite-difference frequency domain (FDFD) simulation model (SI note 2) was employed to provide a numerical solution and reaffirm the trend of experimental data regarding the varying flake thickness under the excitation of a 900 nm source and other wavelengths (Figure S5). To investigate the influence of wavelength on SHG behavior for different thickness flakes, two different flakes having a thickness of 12.2 and 60 nm were measured under increasing excitation wavelengths, ranging from 830 nm to 1040 nm (Figure 2f). The 12.2 nm thick flake exhibited the strongest emission at an excitation wavelength of 1040 nm and experienced an overall increasing trend with increased wavelength. On the other hand, for another flake with 60 nm thickness, the largest emission was observed at a wavelength of 870nm, and the overall emission would decrease with longer wavelength. A comparison between the SHG response of the 12.2 nm flake divided by the SHG response of the 60 nm thick flake response revealed an increasing trend (denoted as enhancement factor), where the shared second order

nonlinear optical susceptibility of tellurene results in consistent responses at given excitation wavelengths, but the thickness effect results in differing SHG magnitudes.

SHG behavior of post-growth treated tellurene nanoflakes

Given that the proper thickness of a tellurene flake is an important factor in optimizing the nonlinear optical performance, an effective method for modulating the flake thickness can further influence the application prospects and value of 2D tellurene. Herein, hydrogen (H^+) plasma was employed in this work as a post-growth treatment process to systematically etch and reduce tellurene flake thickness. A similar approach was previously demonstrated to fabricate few layered BP[45]. When the H^+ plasma treatment process starts, H^+ collide and uniformly distribute on the top surface of the thick Te flakes, accordingly, continuously accelerated H^+ react with the surface Te atoms and form H_2Te gas. As H_2Te gas can ultimately decompose into H_2 and Te at room temperature[46], this etching method effectively realizes the controllable removal of undesired molecules, thus reducing the thickness of the flakes (Fig 3a). Due to the dynamic equilibrium state of the reaction between H^+ and Te during the treatment process, thickness modulation provides a reliable etching rate and homogeneity, as confirmed by characterization tests conducted prior to and after the treatment (Fig S6). As illustrated in Fig 3b, through monitoring every etching treatment, the same treatment duration produces a comparable etched thickness, leading to an overall removal rate with a linear relationship between the etched depth and treatment duration. At the same time, to ensure the nonlinear optical properties of treated flakes, the crystallization and purity were examined by Raman tests after each treatment. The spectra clearly showed three separate Raman active modes, and the sharp peaks suggest the high crystal clarity of the Te flakes following the thinning down process (Figure 3b). A significant blue shift for the E_2 and

A_1 modes can be observed when the flake thickness was reduced, because of hardened vibration modes induced by the modulation of interchain and intrachain interactions[21,30,47]. This corresponds well with the results of untreated flakes (Fig S1b) in previous reports[21,48].

Given that the examination of SHG performance during the etching process can only provide limited insights regarding the emission variation induced by the reduced thickness of treated sample, a treated tapered-face flake serves as a great platform for investigating varying thickness and related SHG behavior (Figure 4a). After H^+ treatment, the tapered-face tellurene flake still has high crystallinity and purity, regardless of the thickness change along the length of the flake (Figure S7). The SHG intensity distribution over the flake surface was imaged under different excitation wavelengths, as presented in Figure 4b. As the wavelength increased from 830 to 1040 nm, two strong emission regions with distinct physical thickness difference had obvious variations in SHG intensity. When the excitation wavelength was larger than 900 nm, the local emission maximum named 'peak A' had less emission intensity than that of another local maximum 'peak B', whose corresponding thickness are around 67 nm and 17 nm, respectively (Figure 4c). It is worth noting that even though the treated sample surface is no longer smooth as compared to prior to H^+ etching, the treated flake remains responsive to changes in excitation wavelength, where the positions of the two peaks both exhibited a slight shift towards the thicker region of the flake as the excitation wavelength became longer. For comparison, the FDFD method was utilized to simulate the SHG profiles using the smooth surface obtained from the effective thickness of the treated flake, as depicted in Figure 4d. Two emission peaks were observed in the simulation as well. Evidently, these peaks displayed a migration pattern similar to that observed for the

treated flake, wherein as the wavelength was altered from 830 to 1040 nm, both Peak A and Peak B simoutanesously move towards the thicker region. After the collection of more SHG profiles (Figure S5), the simulated and expriemental results exhibit a positive linear relationship between peak location and wavelength, following thickness dependent behaviors. Notebly, despite the different root mean square value of roughness (RMS) in the regions of A and B peaks, the larger RMS B peak (3.81 ± 0.11 nm) and smaller RMS A peak (2.65 ± 0.16 nm) both exhibit the same SHG behaviors in response to exciation wavelength. The location of peaks suggests that the roughness does not change the optimized thickness for emission. Meanwhile, comparing the migration distance of peaks between two sets of profiles reveals that the roughened surface of treated samples induced by plasma etching shows no major disparity from the smooth flake, in terms of its thickness-dependent sensitivity to changes in excitation wavelength. As shown in Figure 4e, the ratio of intensities from the two peaks reveals that the treated flake has great agreement with the ratio obtained from simulated results of the smooth flake, further elucidating the thickness dependent nominal SHG emission relationship. Therefore, the roughness on the treated flake does not cause an increase in scattering and light trapping, resulting in the insignificant influence on the light absorption, the phase matching and light propagation invloved in the SHG emission[49,50]. The emission efficiency of a treated flake is equvalent to the optimized performance from the untreated flake of the various thickness under corresponding wavelengths.

Conclusion

This work provided a comprehensive investigation into the SHG performance of 2D tellurene flakes fabricated by confined space PVD growth, in addition to post-process

plasma treatment SHG performance. The tellurene flakes exhibited extraordinary SHG emission and had strong dependence on the flake thickness and excitation wavelength. In addition, the application of plasma treatment effectively reduced flake thickness, enabling tellurene to overcome the limitation of thickness and wavelength interaction. Tellurene's SHG emission is experimentally observed to be about two orders of magnitudes greater than monolayer TMDC counterparts at a larger thickness. This finding offers a fundamental concept to produce all-round 2D tellurium flakes with high SHG emission at various wavelengths. As a result, tellurene as an excellent nano-scaled NLO material will find valuable applications in NLO devices, such as electro-optical switches, frequency converters, phase matching and light signal modulators.

Methods

Synthesis and thinning of 2D tellurene crystals: 5mg Tellurium pellets (99.9%, Sigma Aldrich) as precursors were placed in a porcelain boat in the center of the furnace. Two 275 nm SiO_2/Si substrates were in the face-to-face contact configuration and placed on another porcelain boat 18-20 cm downstream from the heating zone, at the insulating zone of the furnace. Prior to the growth, the quartz tube was vacuumed and refilled with high purity argon gas at a gas flow rate of 500 standard cubic centimeters per minute (sccm) for 5 minutes each time, to eliminate as much residual air as possible. After repeating the purging process several times, the tellurium pellets in the heating zone were heated to 450°C with the temperature rise gradient set at 20°C/min. and then held at 450°C for 20 minutes. A mixture of argon and hydrogen (5% hydrogen) at a total gas flow rate of 50 sccm was used as the carrier atmosphere and reducing atmosphere, and the pressure inside of the quartz tube remained vacuum throughout the deposition process. When the growth was completed, the furnace was cooled down naturally and a large amount of pristine two-dimensional tellurene nanoflakes were obtained on both substrates. Plasma-assisted post growth thinning process was carried out by treating the Te flakes via the ICP-RIE (Samco 400iP) with H_2 gas source. The treatment process was operated with ICP power 10W, bias power 5W, 30 sccm gas flow rate and the vacuum condition of 10Pa to achieve the etching rate around 2.6 nm/s, where moderate treatment conditions enable uniform and controllable etching rate.

Crystal characterization: The Raman spectra of Te flakes were measured via a Raman spectrometer (Horiba Jobin-Yvon T64000 Micro-Raman/Micro-PL) with 532 nm laser incident. To measure the angle-resolved Raman spectra, the linear polarizers were in front of the sample and spectrometer, and a half-wave plate was placed in the path to rotate the

incident direction in 5° steps. Temperature dependent Raman spectra of a Te flake were obtained by using an external temperature controller to change the sample temperature inside of the Linkam chamber.

Imaging of tellurene flakes: Optical images of tellurene flakes were taken by optical microscope (Nikon Eclipse LV150NL). The topologic images and height profiles were captured by using AFM (Bruker Dimension Icon). All measurements were performed conducted in Scanasyst Air experiment mode and soft cantilevers used was Scanasyst-Air, whose nominal spring constant k and nominal tip radius are 0.4 N/m and 2 nm, respectively.

SHG measurements: SHG measurements are performed using Zeiss 780 Confocal Microscopy equipped with a tunable pulse laser Ti:Sapphire laser with a pulse width of 150 fs and a repetition rate of 80 MHz is used in the fundamental laser field. The sample was excited and measured under a 50× confocal objective lens (NA= 0.85), and test results were collected in the reflection mode at a fundamental laser wavelength of 900 nm, and a laser with a tunability range of (820nm–1040nm) was employed for wavelength-dependent SHG measurements. For polarization resolved SHG, an analyzer (polarizer), which was parallel to the polarization of the pump beam, was used to select the polarization component of the SH radiation and the sample was placed on a rotational stage to collect the SH response in terms of polarization angles. All data are collected via Zeiss 780 Confocal Microscopy for optical characterization measurements were processed and analyzed by image processing software, Zen 3.4 (blue edition).

Acknowledgment

The authors acknowledge funding support from ANU PhD student scholarship, Australian Research Council (ARC; numbers DP220102219, DP180103238, LE200100032) and ARC Centre of Excellence in Quantum Computation and Communication Technology (CE170100012), and National Heart Foundation (ARIES ID: 35852). B. L. would like to acknowledge the support from Centre of Advanced Microscopy (CAM), Australian National University.

Author contribution

Y.L. conceived and supervised this study; B.L., K.L., Z.L. prepared conducted the sample fabrication and process; B.L. and A.R.K. conducted the SHG measurements and data analysis; B.L performed AFM tests; B.L., K.L., A.R.K., X.S. S.R. conducted Raman tests; Q.Z. and Z.Y. performed numerical simulation model; Y.L., B.L., K.L. and T.Y. prepared the manuscript. All authors contributed to the project.

Reference List

1 Li, W.-L. *et al.* The B35 Cluster with a Double-Hexagonal Vacancy: A New and More Flexible Structural Motif for Borophene. *Journal of the American Chemical Society* **136**, 12257-12260 (2014).

2 Tao, L. *et al.* Silicene field-effect transistors operating at room temperature. *Nature Nanotechnology* **10**, 227-231 (2015).

3 Ni, Z. *et al.* Tunable Bandgap in Silicene and Germanene. *Nano Letters* **12**, 113-118 (2012).

4 Liu, H. *et al.* Phosphorene: An Unexplored 2D Semiconductor with a High Hole Mobility. *ACS Nano* **8**, 4033-4041 (2014).

5 Zhang, S., Yan, Z., Li, Y., Chen, Z. & Zeng, H. Atomically Thin Arsenene and Antimonene: Semimetal-Semiconductor and Indirect-Direct Band-Gap Transitions. *Angewandte Chemie* **127**, 3155-3158 (2015).

6 Mannix, A. J., Kiraly, B., Hersam, M. C. & Guisinger, N. P. Synthesis and chemistry of elemental 2D materials. *Nature Reviews Chemistry* **1** (2017).

7 Zhu, Z. *et al.* Multivalency-Driven Formation of Te-Based Monolayer Materials: A Combined First-Principles and Experimental study. *Physical Review Letters* **119**, 106101 (2017).

8 Huang, X. *et al.* Epitaxial Growth and Band Structure of Te Film on Graphene. *Nano Letters* **17**, 4619-4623 (2017).

9 Zhu, Y.-J., Wang, W.-W., Qi, R.-J. & Hu, X.-L. Microwave-Assisted Synthesis of Single-Crystalline Tellurium Nanorods and Nanowires in Ionic Liquids. *Angewandte Chemie International Edition* **43**, 1410-1414 (2004).

10 Bottom, V. E. The Hall Effect and Electrical Resistivity of Tellurium. *Science* **115**, 570-571 (1952).

11 Liu, J.-W., Zhu, J.-H., Zhang, C.-L., Liang, H.-W. & Yu, S.-H. Mesostructured Assemblies of Ultrathin Superlong Tellurium Nanowires and Their Photoconductivity. *Journal of the American Chemical Society* **132**, 8945-8952 (2010).

12 Peng, H., Kioussis, N. & Snyder, G. J. Elemental tellurium as a chiral p-type thermoelectric material. *Physical Review B* **89**, 195206 (2014).

13 Hermann, J. P., Quentin, G. & Thuillier, J. M. Determination of the d14 piezoelectric coefficient of tellurium. *Solid State Communications* **7**, 161-163 (1969).

14 Cheng, M., Wu, S., Zhu, Z.-Z. & Guo, G.-Y. Large second-harmonic generation and linear electro-optic effect in trigonal selenium and tellurium. *Physical Review B* **100** (2019).

15 Wagnière, G. H. & Woźniak, S. in *Encyclopedia of Spectroscopy and Spectrometry (Third Edition)* (eds John C. Lindon, George E. Tranter, & David W. Koppenaal) 375-387 (Academic Press, 2017).

16 Cai, X., Han, X., Zhao, C., Niu, C. & Jia, Y. Tellurene: An elemental 2D monolayer material beyond its bulk phases without van der Waals layered structures. *Journal of Semiconductors* **41** (2020).

17 Zhou, G. *et al.* High-Mobility Helical Tellurium Field-Effect Transistors Enabled by Transfer-Free, Low-Temperature Direct Growth. *Adv Mater*, e1803109 (2018).
18 Wu, W., Qiu, G., Wang, Y., Wang, R. & Ye, P. Tellurene: its physical properties, scalable nanomanufacturing, and device applications. *Chem Soc Rev* (2018).
19 Gao, Z., Tao, F. & Ren, J. Unusually low thermal conductivity of atomically thin 2D tellurium. *Nanoscale* **10**, 12997-13003 (2018).
20 Shi, Z. *et al.* Two-Dimensional Tellurium: Progress, Challenges, and Prospects. *Nanomicro Lett* **12**, 99 (2020).
21 Wang, Y. *et al.* Field-effect transistors made from solution-grown two-dimensional tellurene. *Nature Electronics* **1**, 228-236 (2018).
22 Qiu, G. *et al.* Thermoelectric Performance of 2D Tellurium with Accumulation Contacts. *Nano Letters* **19**, 1955-1962 (2019).
23 Qiu, G. *et al.* Quantum Transport and Band Structure Evolution under High Magnetic Field in Few-Layer Tellurene. *Nano Letters* **18**, 5760-5767 (2018).
24 Amani, M. *et al.* Solution-Synthesized High-Mobility Tellurium Nanoflakes for Short-Wave Infrared Photodetectors. *ACS Nano* **12**, 7253-7263 (2018).
25 Peng, M. *et al.* Blackbody-sensitive room-temperature infrared photodetectors based on low-dimensional tellurium grown by chemical vapor deposition. *Science Advances* **7**, eabf7358 (2021).
26 Deckoff-Jones, S., Wang, Y., Lin, H., Wu, W. & Hu, J. Tellurene: A Multifunctional Material for Midinfrared Optoelectronics. *ACS Photonics* **6**, 1632-1638 (2019).
27 Zhang, F. *et al.* Broadband nonlinear absorption properties of two-dimensional hexagonal tellurene nanosheets. *Nanoscale* **11**, 17058-17064 (2019).
28 Wu, L. *et al.* 2D Tellurium Based High-Performance All-Optical Nonlinear Photonic Devices. *Advanced Functional Materials* **29** (2019).
29 Autere, A. *et al.* Nonlinear Optics with 2D Layered Materials. *Adv Mater* **30**, e1705963 (2018).
30 Rao, G. *et al.* Robust Piezoelectricity with Spontaneous Polarization in Monolayer Tellurene and Multilayer Tellurium Film at Room Temperature for Reliable Memory. *Adv Mater* **34**, e2204697 (2022).
31 Zhao, X. *et al.* Controllable synthesis of high-quality two-dimensional tellurium by a facile chemical vapor transport strategy. *iScience* **25**, 103594 (2022).
32 Huang, B. *et al.* High-quality two-dimensional tellurium flakes grown by high-temperature vapor deposition. *Journal of Materials Chemistry C* **9**, 14394-14400 (2021).
33 Wang, Q. *et al.* Van der Waals Epitaxy and Photoresponse of Hexagonal Tellurium Nanoplates on Flexible Mica Sheets. *ACS Nano* **8**, 7497-7505 (2014).
34 Liu, H. *et al.* Tellurium-assisted and space-confined growth of graphene single crystals. *Carbon* **173**, 54-60 (2021).
35 Chen, C.-C. *et al.* Growth of Large-Area Graphene Single Crystals in Confined Reaction Space with Diffusion-Driven Chemical Vapor Deposition. *Chemistry of Materials* **27**, 6249-6258 (2015).
36 Li, L., Liu, J., Zeng, M. & Fu, L. Space-confined growth of metal halide perovskite crystal films. *Nano Research* **14**, 1609-1624 (2021).

37 Sen, S. *et al.* Synthesis of Tellurium Nanostructures by Physical Vapor Deposition and Their Growth Mechanism. *Crystal Growth & Design* **8**, 238-242 (2008).
38 Wang, C. *et al.* Anisotropic Properties of Tellurium Nanoflakes Probed by Polarized Raman and Transient Absorption Microscopy: Implications for Polarization-Sensitive Applications. *ACS Applied Nano Materials* **5**, 1767-1774 (2022).
39 Gan, X. *et al.* Giant and Anisotropic Nonlinear Optical Responses of 1D van der Waals Material Tellurium. *Advanced Optical Materials* **8** (2020).
40 Shi, J. *et al.* 3R MoS2 with Broken Inversion Symmetry: A Promising Ultrathin Nonlinear Optical Device. *Adv Mater* **29** (2017).
41 Khan, A. R. *et al.* Optical Harmonic Generation in 2D Materials. *Advanced Functional Materials* **32** (2021).
42 Khan, A. R. *et al.* Direct Measurement of Folding Angle and Strain Vector in Atomically Thin WS2 Using Second-Harmonic Generation. *ACS Nano* **14**, 15806-15815 (2020).
43 Kumar, N. *et al.* Second harmonic microscopy of monolayer MoS2. *Physical Review B* **87** (2013).
44 Mishina, E. *et al.* Observation of two polytypes of MoS2 ultrathin layers studied by second harmonic generation microscopy and photoluminescence. *Applied Physics Letters* **106** (2015).
45 Pei, J. *et al.* Producing air-stable monolayers of phosphorene and their defect engineering. *Nat Commun* **7**, 10450 (2016).
46 Dittmer, D. C. in *Encyclopedia of Reagents for Organic Synthesis* (2001).
47 Pine, A. S. & Dresselhaus, G. Raman Spectra and Lattice Dynamics of Tellurium. *Physical Review B* **4**, 356-371 (1971).
48 Yang, D.-Q. *et al.* Band Structure and Lattice Vibration of Elemental Tellurium Investigated by Temperature‐Dependent Mid‐and‐Far Infrared Transmission and Raman Spectroscopy. *physica status solidi (b)* **259** (2022).
49 Matos, O. M., Torchia, G. A., Vaveliuk, P., Bilmes, G. M. & Tocho, J. O. Surface roughness dependence of noncollinear phase matching. *Journal of Optics A: Pure and Applied Optics* **4**, 130 (2002).
50 Li, J.-S., Tang, Y., Li, Z.-T., Ding, X.-R. & Li, Z. Study on the optical performance of thin-film light-emitting diodes using fractal micro-roughness surface model. *Applied Surface Science* **410**, 60-69 (2017).
51 Martin, R. M., Lucovsky, G. & Helliwell, K. Intermolecular bonding and lattice dynamics of Se and Te. *Physical Review B* **13**, 1383-1395 (1976).
52 Wang, X. *et al.* Highly anisotropic and robust excitons in monolayer black phosphorus. *Nature Nanotechnology* **10**, 517-521 (2015).
53 Ling, X. *et al.* Anisotropic Electron-Photon and Electron-Phonon Interactions in Black Phosphorus. *Nano Letters* **16**, 2260-2267 (2016).
54 Wu, W., Qiu, G., Wang, Y., Wang, R. & Ye, P. Tellurene: its physical properties, scalable nanomanufacturing, and device applications. *Chem Soc Rev* **47**, 7203-7212 (2018).
55 Yan, R. *et al.* Thermal Conductivity of Monolayer Molybdenum Disulfide Obtained from Temperature-Dependent Raman Spectroscopy. *ACS Nano* **8**, 986-993 (2014).

56 Su, L., Zhang, Y., Yu, Y. & Cao, L. Dependence of coupling of quasi 2-D MoS2 with substrates on substrate types, probed by temperature dependent Raman scattering. *Nanoscale* **6**, 4920-4927 (2014).

57 Anees, P., Valsakumar, M. C. & Panigrahi, B. K. Temperature dependent phonon frequency shift and structural stability of free-standing graphene: a spectral energy density analysis. *2D Materials* **2**, 035014 (2015).

58 Pawbake, A. S., Erande, M. B., Jadkar, S. R. & Late, D. J. Temperature dependent Raman spectroscopy of electrochemically exfoliated few layer black phosphorus nanosheets. *RSC Advances* **6**, 76551-76555 (2016).

59 Zouboulis, E. S. & Grimsditch, M. Raman scattering in diamond up to 1900 K. *Physical Review B* **43**, 12490-12493 (1991).

60 Yan, Z. *et al.* Phonon and thermal properties of exfoliated TaSe2 thin films. *Journal of Applied Physics* **114** (2013).

61 Schinke, C. *et al.* Uncertainty analysis for the coefficient of band-to-band absorption of crystalline silicon. *AIP Advances* **5**, 067168 (2015).

62 Szarvas, T. & Kis, Z. Numerical simulation of nonlinear second harmonic wave generation by the finite difference frequency domain method. *J. Opt. Soc. Am. B* **35**, 731-740 (2018).

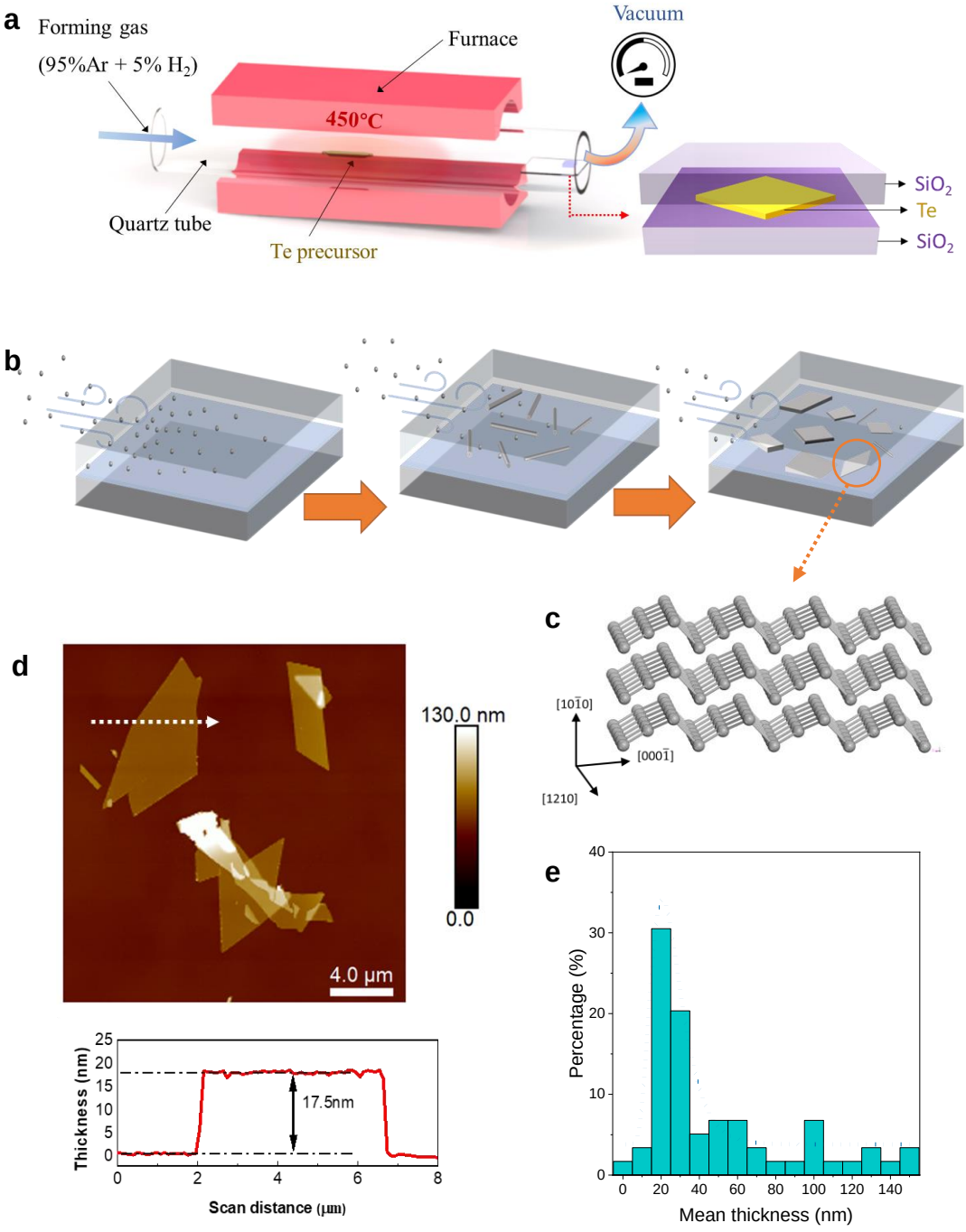
a
Forming gas
(95%Ar + 5% H2)
Furnace
Vacuum
450°C
Quartz tube
Te precursor
SiO2
Te
SiO2
b
c
[10$\bar{1}$0]
[000$\bar{1}$]
[1210]
d
130.0 nm
0.0
4.0 μm
Thickness (nm)
17.5nm
Scan distance (μm)
e
Percentage (%)
Mean thickness (nm)

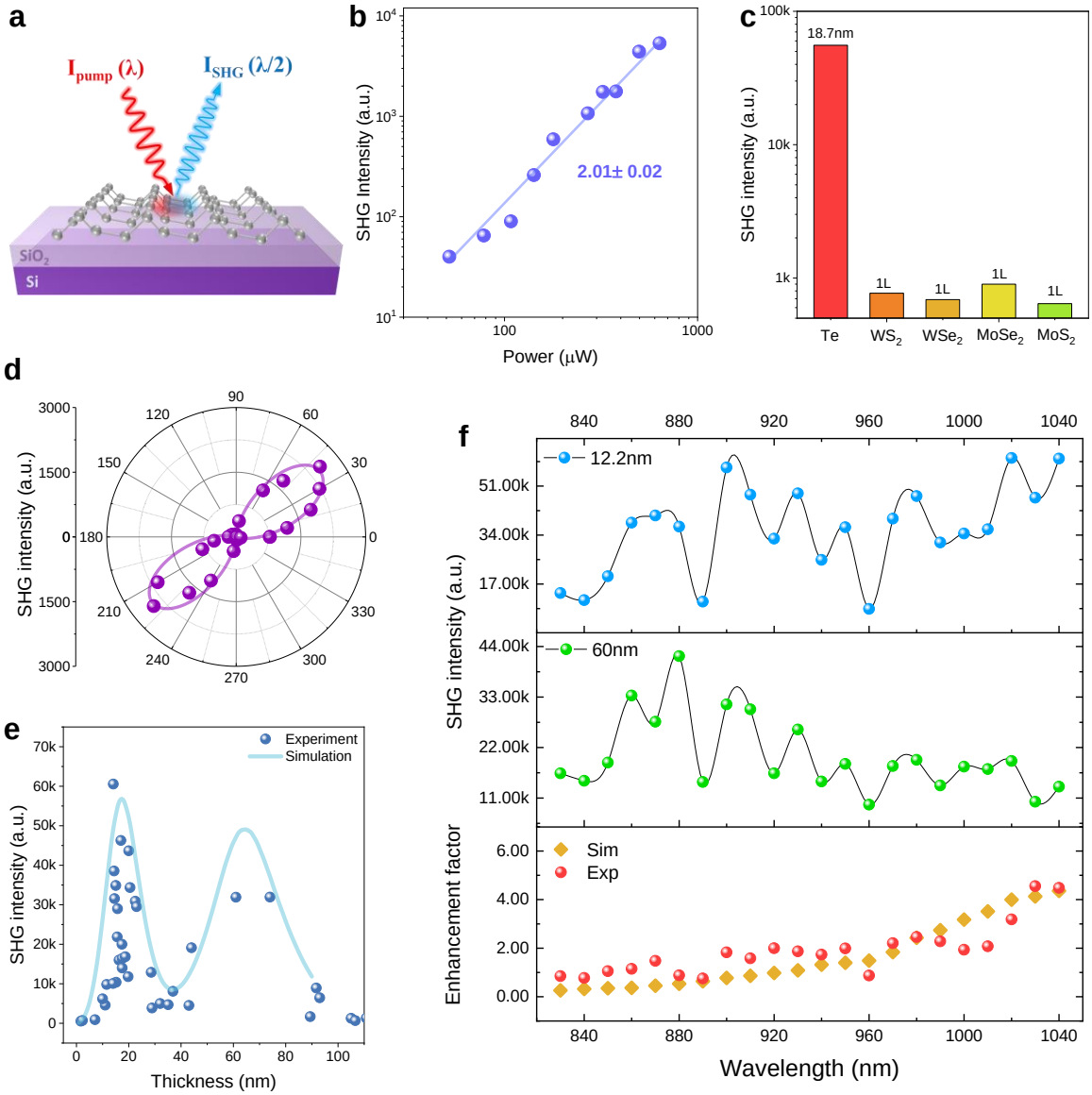
a
I_{pump} (λ)
I_{SHG} (λ/2)
SiO_2
Si
b
SHG Intensity (a.u.)
2.01± 0.02
Power (μW)
c
SHG intensity (a.u.)
18.7nm
1L
Te
WS_2
WSe_2
$MoSe_2$
MoS_2
d
SHG intensity (a.u.)
e
Experiment
Simulation
SHG intensity (a.u.)
Thickness (nm)
f
12.2nm
60nm
SHG intensity (a.u.)
Sim
Exp
Enhancement factor
Wavelength (nm)

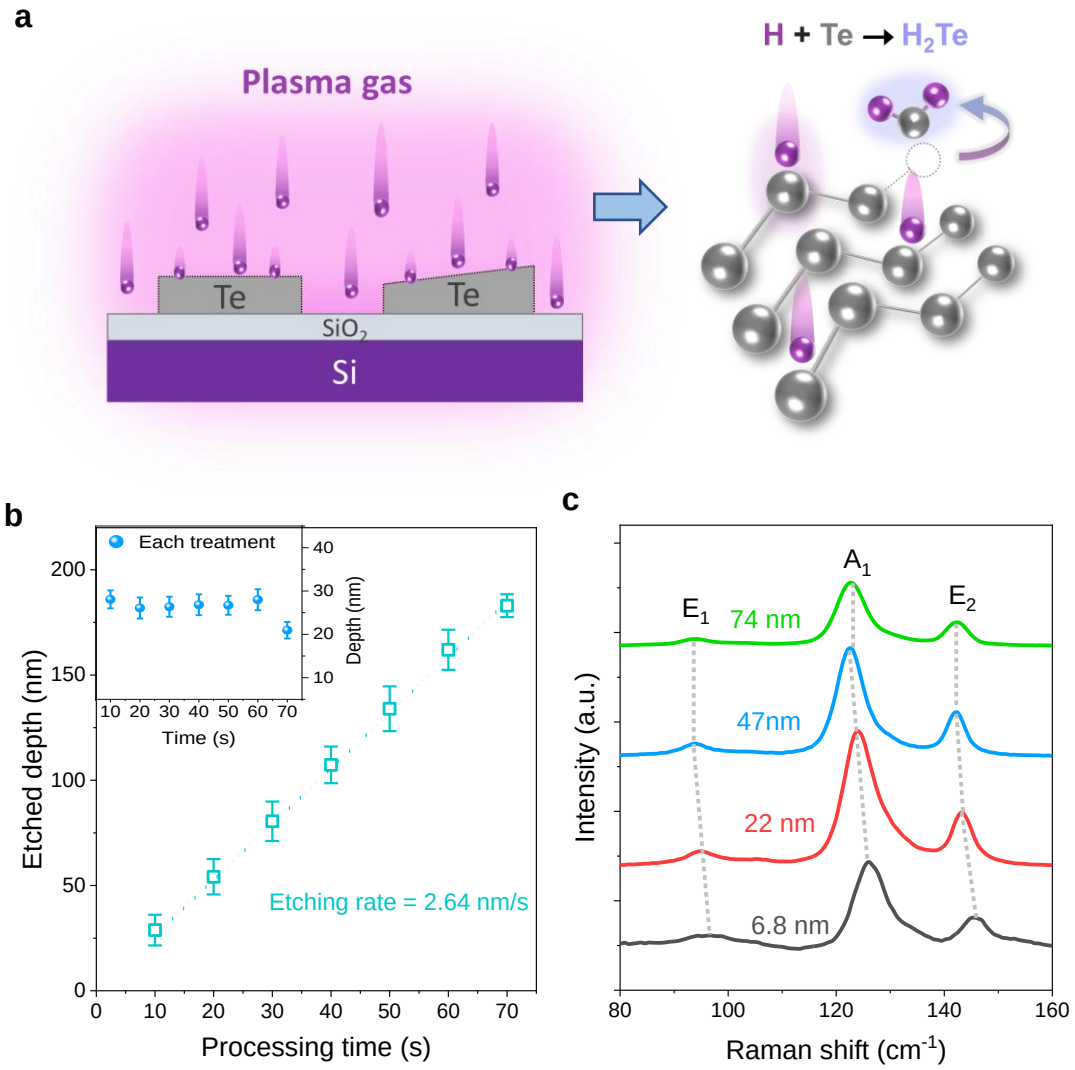
a
Plasma gas
Te
Te
SiO2
Si
H + Te → H2Te
b
Each treatment
Depth (nm)
Time (s)
Etched depth (nm)
Processing time (s)
Etching rate = 2.64 nm/s
c
A1
E1
E2
74 nm
47nm
22 nm
6.8 nm
Intensity (a.u.)
Raman shift (cm-1)

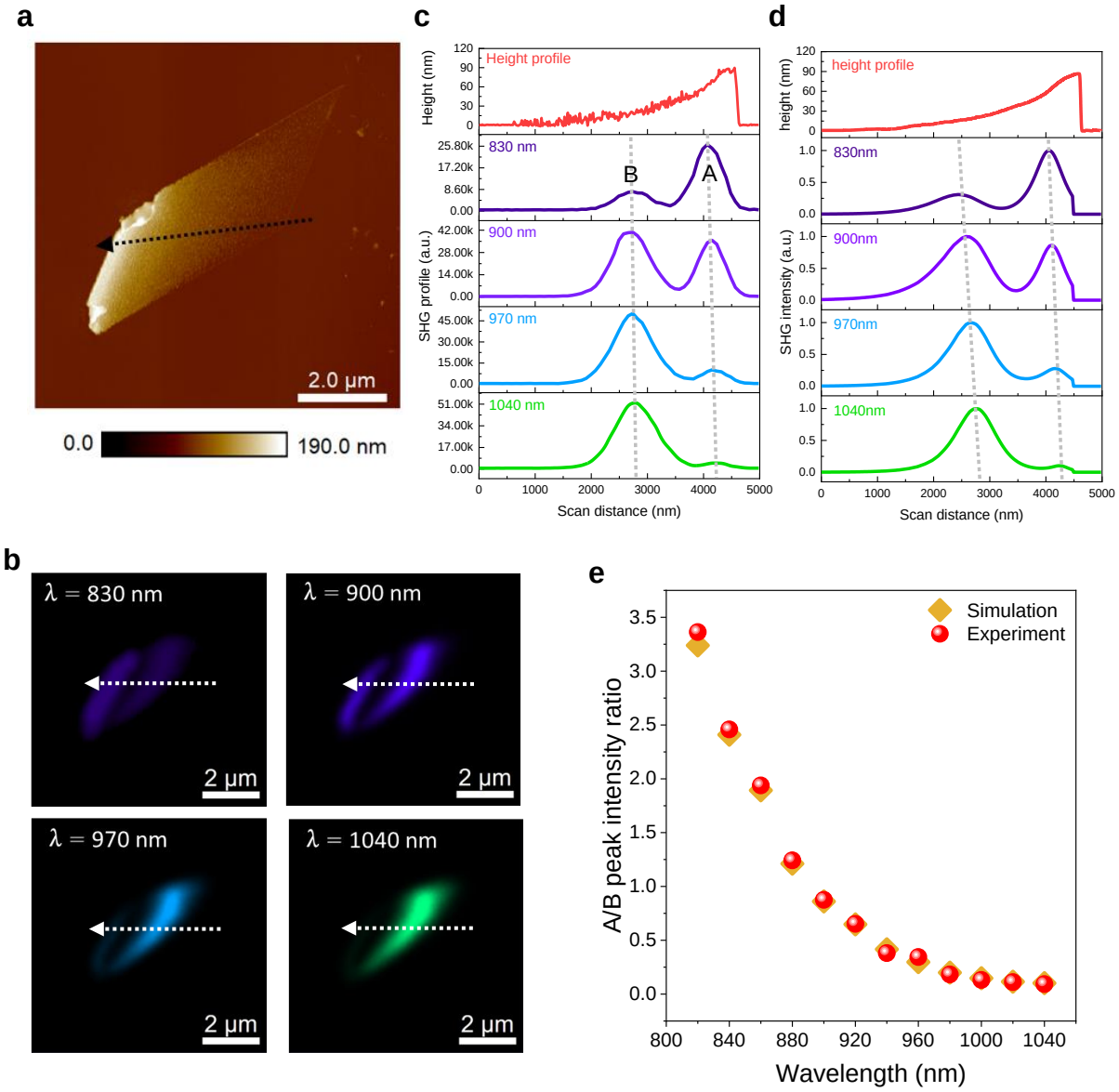
a
2.0 μm
0.0
190.0 nm
c
Height (nm)
Height profile
830 nm
B
A
900 nm
970 nm
1040 nm
SHG profile (a.u.)
Scan distance (nm)
d
height (nm)
height profile
830nm
900nm
970nm
1040nm
SHG intensity (a.u.)
Scan distance (nm)
b
λ = 830 nm
λ = 900 nm
λ = 970 nm
λ = 1040 nm
2 μm
e
Simulation
Experiment
A/B peak intensity ratio
Wavelength (nm)

Figure captions

Figure 1. Two-dimensional Tellurene crystals synthesized with PVD method. (a) Schematic of tellurene flakes grown using the PVD method with a face-to-face contact substrate configuration under vacuum conditions. The face-to-face contact substrate is depicted in the inset. **(b)** Schematic diagram of the growth mechanism and morphologic transition of tellurene flakes realized by delivering vaporized Te into the tight space between substrates, with time and temperature. The light gray spheres, rods and flakes represent Te atoms, nano wires, and thin tellurene flakes, respectively. **(c)** 3D illustration of the atomic structure of a tellurene nano flake. **(d)** Atomic force microscopic (AFM) image of a representative tellurene flake with a thickness of 17.5 nm, where the height profile is extracted along the white dashed line. **(e)** Thickness statistics of tellurene flakes synthesized by our illustrated method, where 15 to 25 nm thick flakes account for approximately 31% of the total tellurene yield.

Figure 2. Characterization of second harmonic generation (SHG) in tellurene flakes. (a) Schematic illustration of SHG mechanism in a 2D tellurene flake, wherein a pump laser reflects of the surface of the at double the frequency and half the wavelength. **(b)** Power dependence of the SHG signal with both axes presented in logarithmic scale. The spheres represent the measured values, while the solid line indicates the linear fit with a slope of 2.01. **(c)** Comparison of SHG emission from a tellurene flake and several monolayer transition metal dichalcogenide flakes under 900 nm illumination. **(d)** Polar plot of angle resolved SHG. **(e)** Analytical (blue solid line) and experimental data (blue solid dots) for SHG emission versus tellurene thickness, ranging from 10 to 90 nm, under an excitation wavelength of 900 nm. **(f)** SHG measurement conducted on two flakes

having thicknesses of 12.2 and 60 nm under varied excitation wavelengths, ranging from 830 to 1040 nm. The enhancement factors suggest two flakes with different thickness show different trends but have consistent response at different wavelength.

Figure 3. Investigation of post-growth thinning process of tellurene flakes via hydrogen plasma. (a) Schematic illustration of plasma-assisted post growth thinning process employed on tellurene flakes, with the thinning process based on the reaction between Te atoms and hydrogen protons in plasma gas. **(b)** Monitoring thickness change and etching rate from consecutive treatments, where the inset demonstrates the constant etching rate from average etch thickness of each treatment with 10s duration. The error bars represent statistical variation from 10 flakes for each treatment group. **(c)** Raman spectra of the processed tellurene flake with the thickness decreasing from 74 nm to 6.8 nm.

Figure 4. SHG behavior of inclined tellurene flakes obtained with the post growth thinning process. (a) AFM image of a tapered-surface tellurene flake after plasma treatment. **(b)** SHG mapping images of the treated flake shown in (a) under the excitation wavelength at 830, 900, 970 and 1040 nm. **(c)** Experimental height profiles and wavelength dependent SHG intensity profiles extracted along black and white dashed lines in (a) and (b), respectively. **(d)** Analytical SHG profiles at corresponding wavelengths based on the mean height values of treated surface in (c). **(e)** Comparison of experimental and analytical SHG variation between the local maxima under various wavelengths.

Supplementary information

Giant Second Harmonic Generation in Two-Dimensional Tellurene Engineered by Plasma Assisted Thinning Process.

Boqing Liu[†], Kun Liang[†], Qingyi Zhou[‡], Zhuoyuan Lu[†], Ahmed Raza Khan[†], Tanju Yildirim[§], Xueqian Sun[†], Sharidya Rahman[†], Yun Liu[‖], Zongfu Yu[‡], Yuerui Lu*[,†,※]

[†] School of Engineering, College of Engineering, Computing & Cybernetics, The Australian National University, Canberra, ACT 2601, Australia

[‡] Department of Electrical and Computer Engineering, University of Wisconsin, WI, Madison, 53706, USA

[§] Center for Functional Sensor & Actuator (CFSN), Research Center for Functional Materials, National Institute for Materials Science (NIMS), 1-1 Namiki, Tsukuba, Ibaraki 305-0044, Japan

[‖] Research School of Chemistry, College of Science, The Australian National University, Canberra, ACT 2601, Australia

[※] ARC Centre of Excellence in Quantum Computation and Communication Technology ANU node, Canberra, ACT 2601, Australia

*To whom correspondence should be addressed: Yuerui Lu (yuerui.lu@anu.edu.au)

Note1: Raman Characterisation

To examine the crystallisation and purity of the tellurene flake synthesised by the confined zone PVD method, comprehensive Raman tests were conducted. As tellurene flakes are formed by the van der Waals interaction existing between adjacent helical chiral chains, this results in three main Raman active modes, E_1 and E_2 modes and a A_1 mode, representing the atom displacements along the $[000\bar{1}]$ chain direction and in & out of the basal plane, respectively [21,51], as indicated in Figure S1a. In Figure S1b, three distinct Raman active modes were clearly identified in the Raman spectra, and the sharp peaks also evidenced the good crystal quality of the tellurene flakes with varying thickness. According to the spectra, there was a significant blue shift for the E_2 and A_1 modes when the flake thickness was reduced from 145 nm to 5.8 nm. The nature of hardened vibration modes could be attributed to the modulation of interchain and intrachain interaction induced by the chiral-chain structure of tellurene. Thinner flakes would result in the stronger long-range Coulombic interaction and thus harden the E_2 vibration mode[21,52]. Meanwhile, the weakened inter-chain van der Waals interaction and enhanced intra-chain covalent interaction both contributed to the stronger restoring forces of Te atoms and a harder out-of-plane A_1 vibration mode[21,30,47]. However, with reduced thickness to around 16 nm, there was an occurrence of the dynamic change induced split of the E_1 mode for transverse (TO) and longitudinal (LO) phonon modes[47], as shown in spectrum of 12 nm flake. The E_1 TO and LO modes experienced blue and red shifts respectively when the thickness ranges from 5.4 to 15.8 nm (Figure S1c), which correspond well with previous reports[21,48]. These shifts of E_1 TO and LO modes are influenced by factors including the increased deformation potential in lattice, enhanced intrachain atomic displacement, symmetry assignment and electronic band structure changes[21,53,54].

Moreover, the symmetry and anisotropic optical properties of tellurene flakes were characterized by the application of angle-resolved Raman spectroscopy. The results showed that the chiral-chain van der Waals structure exhibited a strong in-plane anisotropy. Figure S2a presents the Raman spectra of a 22 nm thick flake extracted under various polarized incident lights. The peak intensities of vibration modes were sensitive to the orientation incident lights and corresponding anisotropic Raman behaviours were observed. The peak intensities of three modes were then extracted and fitted by a Lorentz function and interpreted into the corresponding polar figures (Figure S2b), where the angle-dependent intensity of two E modes and A_1 mode show two-lobe shapes, consistent with previous results[25,38]. In specific, although three modes shared the same polarisation orientation, compared to two E modes, the A_1 mode had largest sensitivity to the relative orientation of the [0001] direction and the polarisation of the excitation laser[21]. This reaffirmed that the tellurene flakes are composed of helical Te atom chains, and both shared the same orientation with the growth direction for [0001].

To further study the thermal expansion and lattice vibration of tellurene, Raman measurements were conducted on a 20nm thick sample in the temperature range of 93K to 313K. With decreased temperatures, all three modes exhibited significant blue shifts as presented in Figure 2e, which are the frequency shifts of phonons ascribed to the related thermal expansion of lattice and anharmonic phonon coupling effect[55-58]. As summarised in Figure 2f, there is a good linear relationship between the peak positions and temperature, which can be well fitted with the following equation[59]

$$\omega(T) = \omega_0 + \chi T \quad (1)$$

where ω_0, χ and T is the Raman peak frequency at 0 K, the first-order temperature coefficients of vibration mode and the test temperature, respectively. As indicated in Figure 2f, the A_1 mode is more sensitive to temperature since its first-order temperature coefficient is largest than the values of E_1 and E_2. Interchain interaction is associated with the chain expansion mode (A_1), whereas intrachain interaction is associated with the bond bending and stretching modes (E_1 and E_2). Tellurium atoms are prone to a minor bind in the direction perpendicular to the spiral molecular chain due to the weak van der Waals forces between the chains. Therefore, the weak vertical vibration of the Te atoms would result in a relatively low thermal expansion coefficient perpendicular to the [0001] direction[19,48]. Furthermore, when compared to graphene and TMD materials[55,60], the lattice thermal expansion is the lowest, showing good thermal stability.

Note 2: Numerical Simulation

2.1 General simulation process

The simulation of the SHG intensity profile is simplified as a 1D problem in this work since the system is homogeneous in both the x and y directions and consists of a set of stacked layers in the z direction. The domain of simulation scenario is constructed based on the experimental conditions as follows: (1) Vacuum; (2) Tellurene flake, with thickness d_1; (3) Silicon dioxide, with thickness $d_2 = 275$ nm; (4) Silicon substrate. The entire simulation process are classified with light pump and SHG emission, which are developed by two different models, transfer matrix method (TMM) and a finite-difference frequency domain (FDFD) simulation, respectively.

For the pump process, a plane wave (wavelength denoted as λ_0, angular frequency denoted as ω) serves as the pump signal. The plane wave includes both x and y-polarization ($|E_x| = |E_y| = 1/\sqrt{2}$). The corresponding electric field distribution $\vec{E}(\omega)$ can be calculated numerically by solving a linear problem. Here transfer matrix method (TMM) is chosen since we're working with stratified layers and the system is homogeneous in both x and y directions. Ignoring the backaction of second-harmonic generation on pump signal, this incident plane wave leads to a field distribution $\vec{E}(\omega)$ inside the simulation domain.

After the electric field $\vec{E}(\omega)$ has been determined, the corresponding second order nonlinear polarization $\vec{P}^{NL}(2\omega)$ can be calculated. This $\vec{P}^{NL}(2\omega)$ will serve as a source, exciting oscillating electromagnetic field with angular frequency 2ω. Since $\vec{P}^{NL}(2\omega)$ oscillates with angular frequency 2ω, electromagnetic waves with angular frequency 2ω

will be generated. For all our simulations, the refractive index of silicon dioxide is fixed as $n = 1.45$. The refractive index of silicon is obtained from literarure[61]. The refractive index of the tellurene flake, as well as its nonlinear susceptibility, have been extracted from DFT simulation results[14]. Now the source is no longer an incident plane wave, but rather a polarization distribution, which requires the employment of the finite-difference frequency domain (FDFD) simulation.

The only assumption here is that the creation of second-harmonic signal has no backaction on the pump signal. Considering that in general, second-harmonic generation process is not very efficient, this assumption remains valid here. In that sense, solving for $\vec{E}(\omega)$ can be carried out before solving for $\vec{E}(2\omega)$, since the two frequencies are almost completely decoupled. It's also possible to treat this problem in a more rigorous way by considering SHG's backaction[62].

2.2 Theoretical models for SHG simulation

Transfer matrix method: pump source

Starting from Maxwell's equations in frequency domain:

$$\nabla \times \vec{H} = -j\omega\epsilon_r\epsilon_0\vec{E},$$

$$\nabla \times \vec{E} = j\omega\mu_0\vec{H}.$$

We've assumed that all materials are isotropic and set $\mu_r = 1$. Here the $e^{-j\omega t}$ time dependence is used. Since we are working in 1D, we can do replacement $\partial/\partial x \to jkx$ and $\partial/\partial y \to jky$. With normal incidence, both k_x and k_y become zero. Thus both E_z and H_z are zero. By eliminating H_x and H_y, we end up with two second-order differential equations:

$$\frac{\partial^2 E_x}{\partial z^2} = -\epsilon_r \frac{\omega^2}{c_0^2} E_x,$$

$$\frac{\partial^2 E_y}{\partial z^2} = -\epsilon_r \frac{\omega^2}{c_0^2} E_y.$$

These are Helmholtz equations, which can be written in a more compact form:

$$\frac{d^2}{dz^2}\begin{pmatrix} E_x \\ E_y \end{pmatrix} - \Omega^2 \begin{pmatrix} E_x \\ E_y \end{pmatrix} = \begin{pmatrix} 0 \\ 0 \end{pmatrix}.$$

By diagonalizing matrix Ω with $\Omega = \mathbf{W}\Lambda\mathbf{W}^{-1}$, we get the general solution.

$$\begin{pmatrix} E_x(z,w) \\ E_y(z,w) \end{pmatrix} = \mathbf{W}e^{\Lambda z}\mathbf{W}^{-1}\vec{a}^{+} + \mathbf{W}e^{-\Lambda z}\mathbf{W}^{-1}\vec{a}^{-}.$$

For a given layer, matrix $\mathbf{W}$ contains many vectors, while each vector corresponds to one eigen-mode inside the layer. By decomposing the electric fields using eigen-modes and applying the boundary condition, we can calculate the S-matrix of the entire system (including all the stacked layers). Then the electric field distribution of pump signal can be extracted.

Nonlinear polarization

Once we've calculated $\vec{E}(\omega)$, the nonlinear polarization $\vec{P}^{NL}(2\omega)$ can be calculated. Suppose we're dealing with one thin Te flake. Its nonlinear susceptibility tensor satisfies:

$$\chi_{111} = -\chi_{122} = -\chi_{212},$$

here indices $1, 2$ correspond to x, y direction. Note that our incident wave goes from z direction and the polarization of its electric field must be inside xy plane.

On the other hand, we cannot detect light with z polarization. Therefore, we may ignore all χ components which include index 3. We change this into another form using $d_{ijk} = \frac{\epsilon_0}{2}\chi_{ijk}$:

$$d_{111} = d_0,\ d_{122} = d_{212} = -d_0.$$

Then we can use the 3×6 tensor form, following the rules:

$$d_{i11} \to d_{i1};\ d_{i22} \to d_{i2};\ d_{i33} \to d_{i3};$$

$$d_{i23}, d_{i32} \to d_{i4};\ d_{i31}, d_{i13} \to d_{i5};\ d_{i12}, d_{i21} \to d_{i6}.$$

This gives

$$d_{11} = d_0,\ d_{12} = d_{26} = -d_0.$$

The relationship between nonlinear polarization $\vec{P}^{NL}$ and pump electric field can be expressed as

$$\begin{pmatrix} P_x(2\omega) \\ P_y(2\omega) \\ P_z(2\omega) \end{pmatrix} = 2\begin{bmatrix} d_{11} & d_{12} & d_{13} & \dots \\ d_{21} & d_{22} & d_{23} & \dots \\ d_{31} & d_{32} & d_{33} & \dots \end{bmatrix}\begin{pmatrix} E_x^2 \\ E_y^2 \\ E_z^2 \\ 2E_yE_z \\ 2E_xE_z \\ 2E_xE_y \end{pmatrix}.$$

Therefore, when ignoring P_z we arrive at

$$P_x(2\omega) = 2d_0\left(E_x^2 - E_y^2\right),\ P_y(2\omega) = -4d_0E_xE_y.$$

Considering that some of our samples are not very thin and all quantities have distribution in z direction, we should write the z dependence explicitly:

$$P_x(z,2\omega) = 2d_0\left(E_x(z,\omega)^2 - E_y(z,\omega)^2\right),\ P_y(2\omega) = -4d_0E_x(z,\omega)E_y(z,\omega).$$

Finite-difference frequency domain: second-harmonic signal

Now that we've calculated the distribution of nonlinear polarization $\vec{P}^{NL}(z,2\omega)$, the corresponding electric field distribution of second-harmonic signal can be calculated directly. Similar to the derivation in TMM part, in this 1D case (normal incidence), Maxwell's equations can be simplified into Helmholtz equation:

$$\frac{\partial^2 E_x(z,2\omega)}{\partial z^2} + \epsilon_r(z)\frac{(2\omega)^2}{c_0^2}E_x(z,2\omega) = -\mu_0(2\omega)^2P_x(z,2\omega),$$

$$\frac{\partial^2 E_y(z,2\omega)}{\partial z^2} + \epsilon_r(z)\frac{(2\omega)^2}{c_0^2}E_y(z,2\omega) = -\mu_0(2\omega)^2P_y(z,2\omega).$$

The above two equations, after discretization, are just two sets of linear equations with form $Ax = b$. Perfectly-matched layers (PMLs) are applied at both ends in order to mimic an outgoing boundary condition without reflection. By solving these linear equations in MATLAB, we can obtain the electric field distribution $\vec{E}(z,2\omega)$. The magnetic field $\vec{H}(z,2\omega)$ can then be derived:

$$H_x(z,2\omega) = -\frac{1}{j(2\omega)\mu_0}\frac{\partial E_y}{\partial z},$$

$$H_y(z,2\omega) = \frac{1}{j(2\omega)\mu_0}\frac{\partial E_x}{\partial z}.$$

Finally, in order to determine the detected second-harmonic signal intensity, we need to calculate the z component of Poynting vector $\vec{S}$:

$$S_z = \frac{1}{2}Re\left[E_x(z,2\omega)H_y^*(z,2\omega) - E_y(z,2\omega)H_x^*(z,2\omega)\right].$$

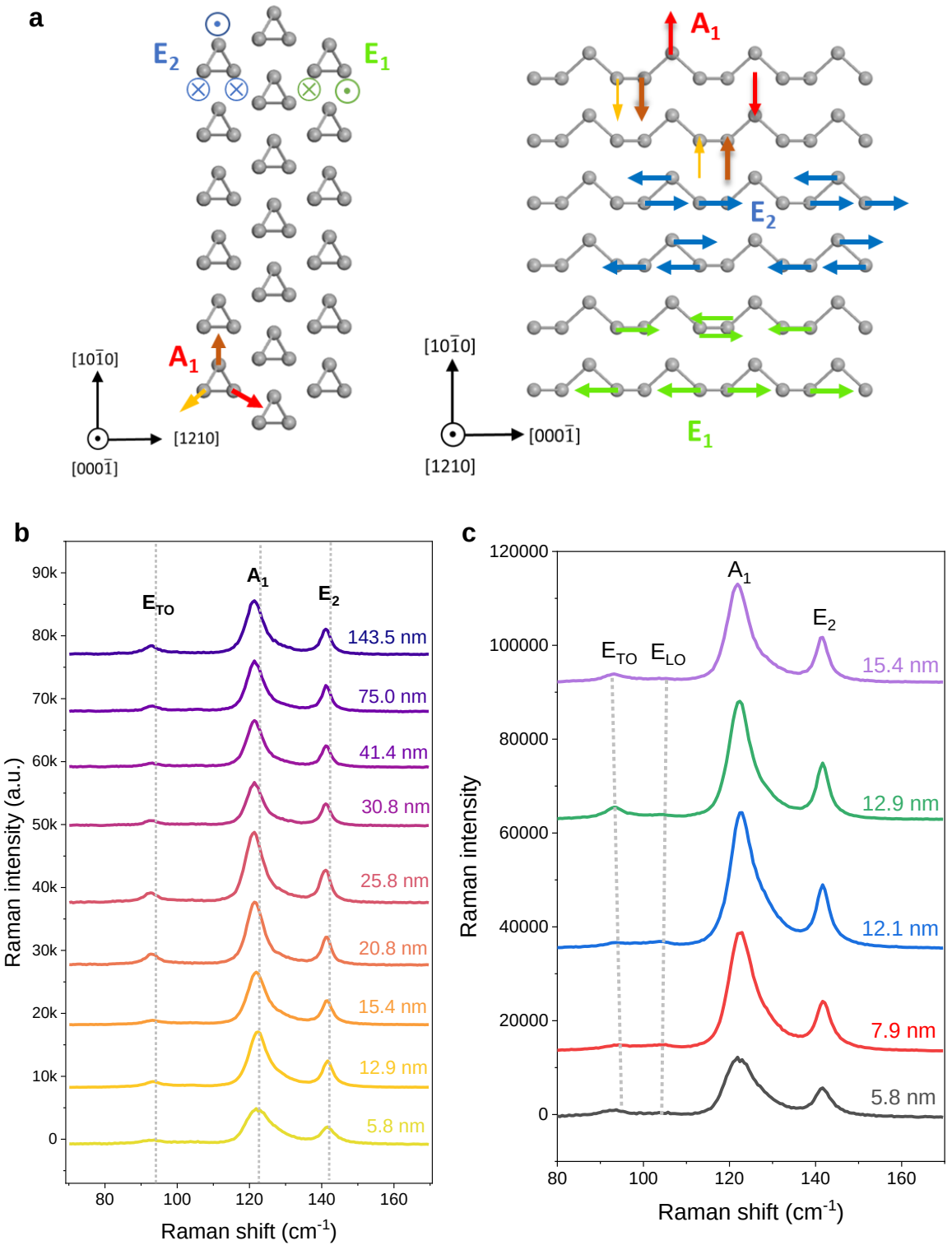

Supplementary Figure 1 | Raman characterization of different thickness tellurene flakes. (a) Schematics of the chiral-chain van der Waals structure of tellurene from the front and side views where three main Raman-active modes have been coded in colors.

(b) Raman spectra for tellurene with different thicknesses ranging from 143 nm to 5.8 nm, where the red shifts of A A_1 and E_2 modes are observed. **(c)** Raman spectra of thin tellurene with E_2 mode transiting into E_{TO} and E_{LO} modes, where the shift difference between the two feature modes is less as the thickness decreases.

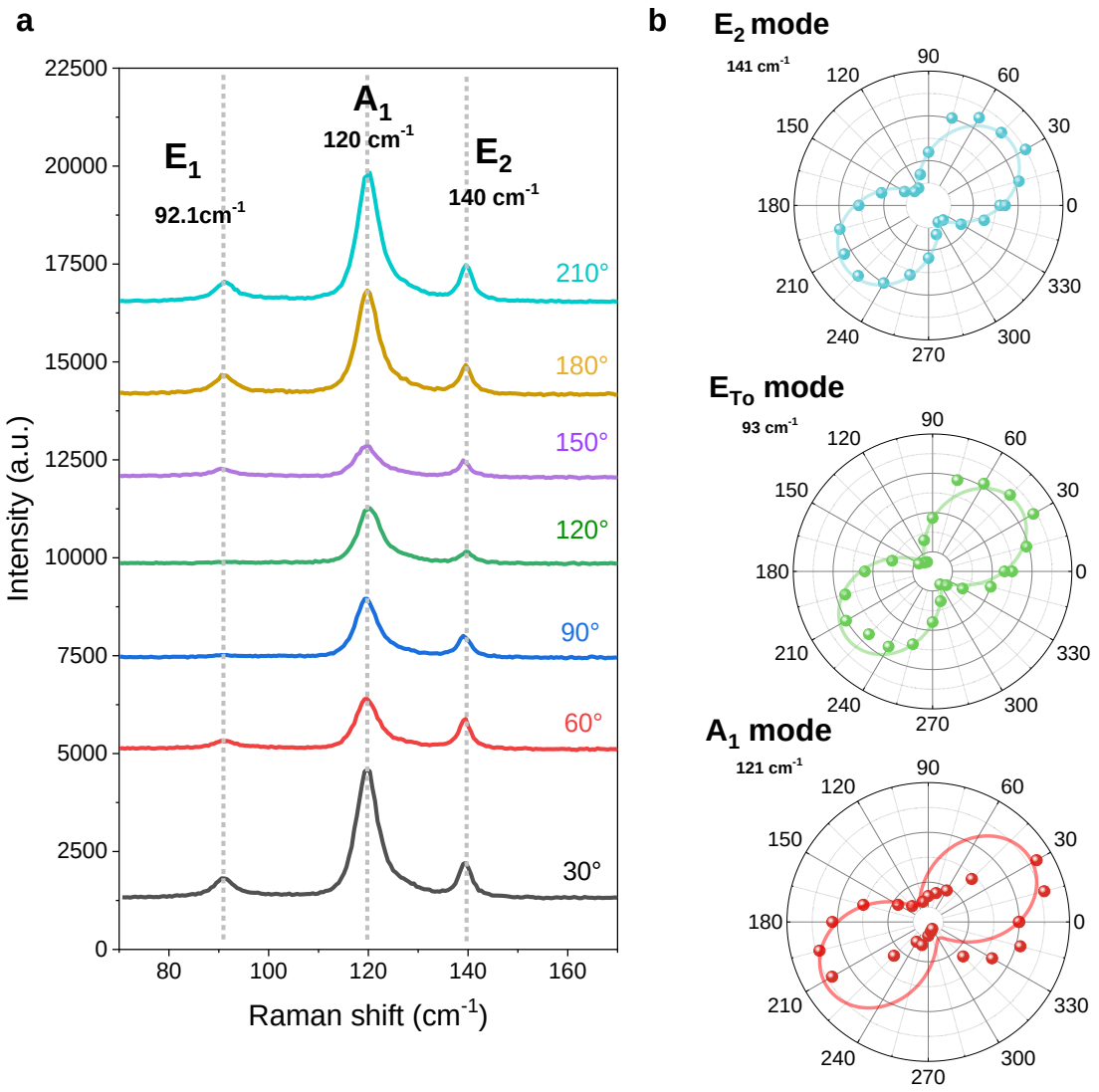

Supplementary Figure 2 | Angle-resolved Raman characterization of the tellurene flake. (a) Angle resolved Raman spectra for a 22-nm-thick flake: evolution with angles between crystal orientation and incident laser polarization. **(b)** Polar plots of Raman intensity corresponding to A_1 and two E modes located at around 93 (E_1), 121 (A_1) and 141 (E_2) cm^{-1}.

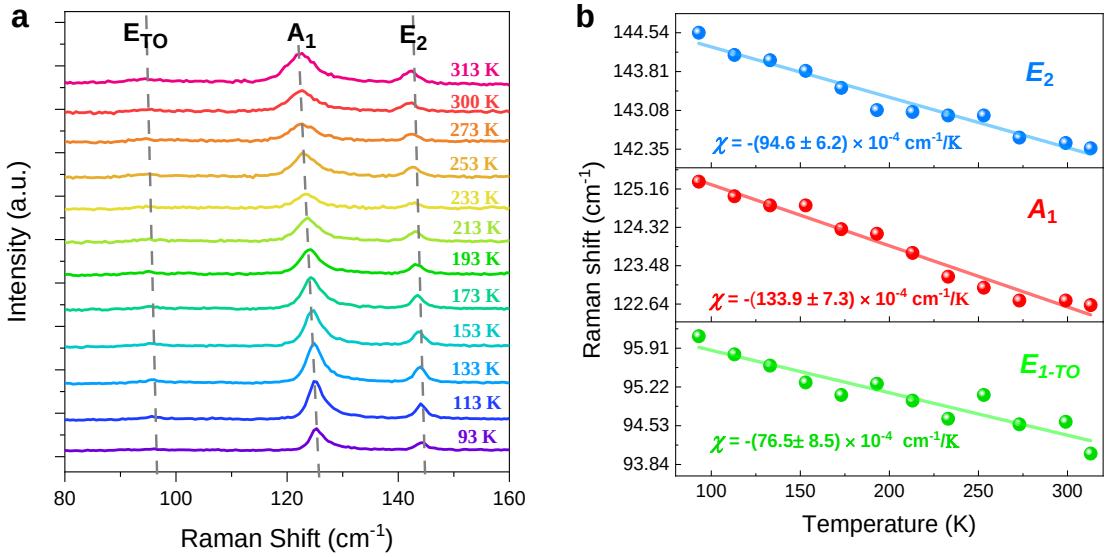

Supplementary Figure 3 | Temperature dependent Raman spectra of the tellurene flake. (a) Temperature-dependent Raman spectra of a 19nm-thick flake, with decreasing temperature leading to an obvious blue shift in three modes. **(b)** Raman peak frequency of A_1 and 2 E modes as a function of temperature, indicating the low thermal conductivity of tellurene flakes.

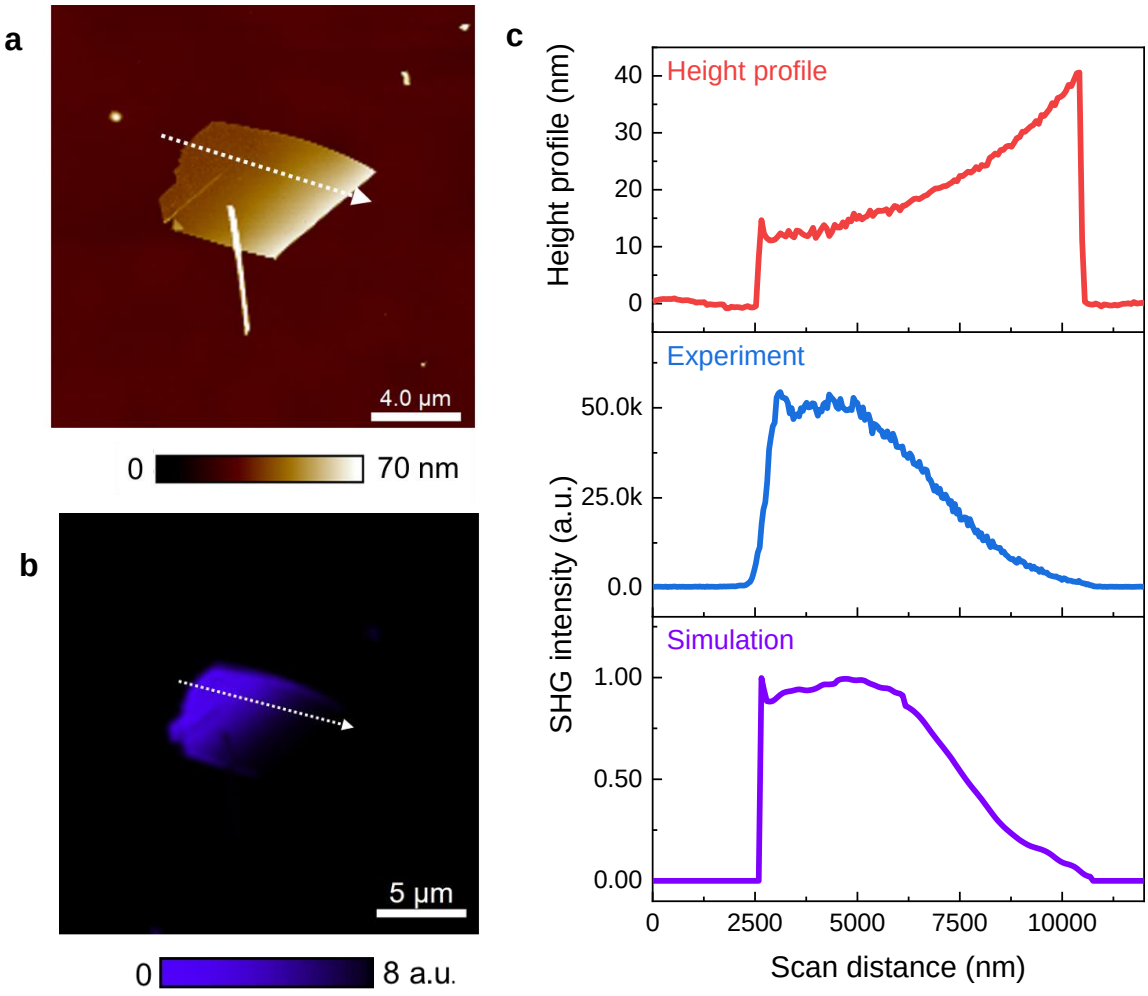

Supplementary Figure 4 | Wavelength-dependent SHG measurements of the tellurene flake with an inclined surface. (a) SHG mapping images of inclined tellurene flakes under the excitation wavelength at 900 nm. **(b)** The experimental SHG intensity profiles extracted along the white dash lines in (a) at corresponding wavelengths, indicating the variation of SHG intensity is determined by the sample thickness and excitation wavelength. **(c)** Theoretical SHG intensity profiles at different wavelengths according to the experimental height profile of the tellurene flake sample in Figure 2e and f, all of which show good agreement with experimental results.

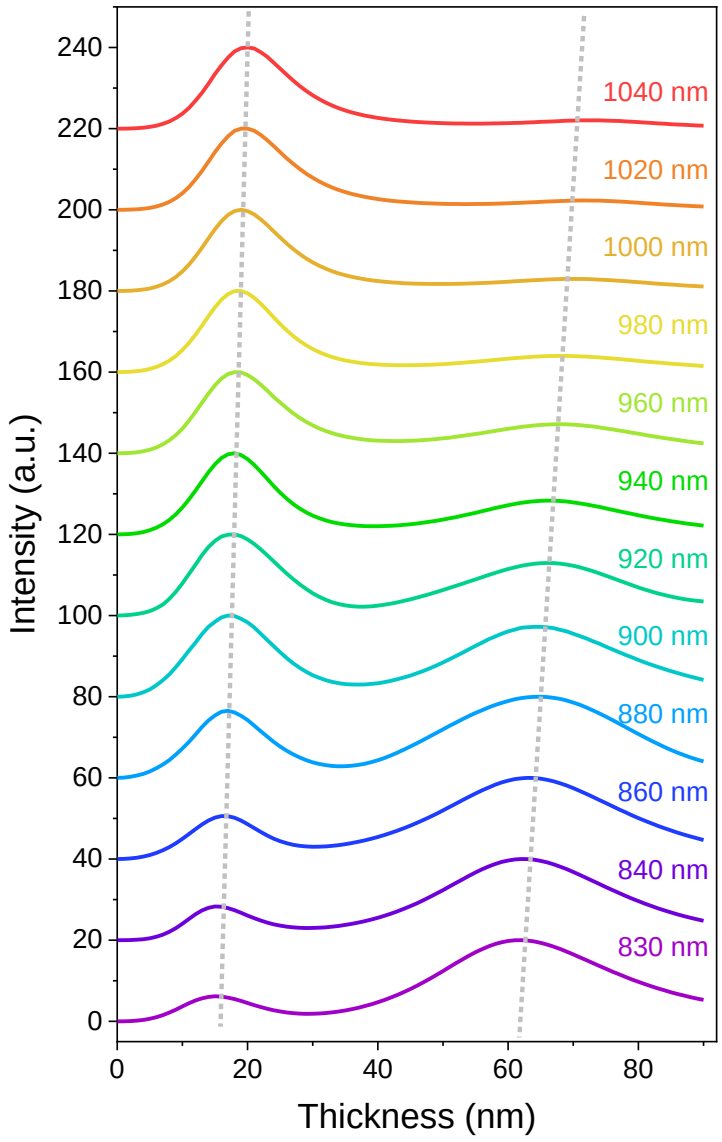

Supplementary Figure 5 | Theoretical thickness-dependent SHG as function of excitation wavelength ranging from 830 nm to 1040nm. The largest SH emission at different excitation wavelengths exhibits great sensitivity to the thickness, where longer wavelengths (> 900 nm) lead to higher emission efficiency in thinner flake, while thicker flake will have larger emission with shorter wavelength excitation (< 900 nm). Furthermore, in comparison to the demand for the highest SH emission for the thicker region at different wavelengths, thin flakes (<20nm) are thought to provide steady

emission output given the low sensitivity to the excitation wavelength and thickness correlation, which indicate the absorption process dominate the SHG performance of thin flakes.

Supplementary Figure 6 | Comparison of tellurene flakes before and after hydrogen plasma thinning process. (a) Optical microscopic images of the tellurene flakes with similar thickness before and after the hydrogen plasma thinning process, where the scale bar in the image is 10μm. **(b)** Raman spectra obtained from tellurene flakes presented in (a) before they experienced plasma treatment, where the comparable thickness of the flakes is confirmed by the similar Raman shift locations of three feature peaks. **(c)** The Raman spectra of the corresponding tellurene flakes after plasma treatment, where reduced thickness exhibited hardened A_1 and E_2 vibration modes, acting as clear blue shifts in the peak locations. **(d)** Comparison of Raman shift difference between the A_1 and E_2 vibration modes before and after the etching process; the smaller shift difference retrieved from treated samples suggests the thickness was effectively reduced, as the relatively closer locations of A_1 and E_2 vibration modes only exist in thinner flakes, which agrees with the published thickness-dependent Raman results. **(e)** The summary of the Raman shift difference in the A_1 and E_2 vibration modes before and after the thinning process; the A_1 mode of three samples experience 5.95 cm^{-1}, 5.99 cm^{-1} and 6.52 cm^{-1} for S1, S2 and S3, respectively, while their E_2 modes possess comparable shift differences with 3.34 cm^{-1}, 3.37 cm^{-1} and 3.60 cm^{-1}, which indicates that the etching process is believed to create constant etched depth and uniform coverage on the surface.

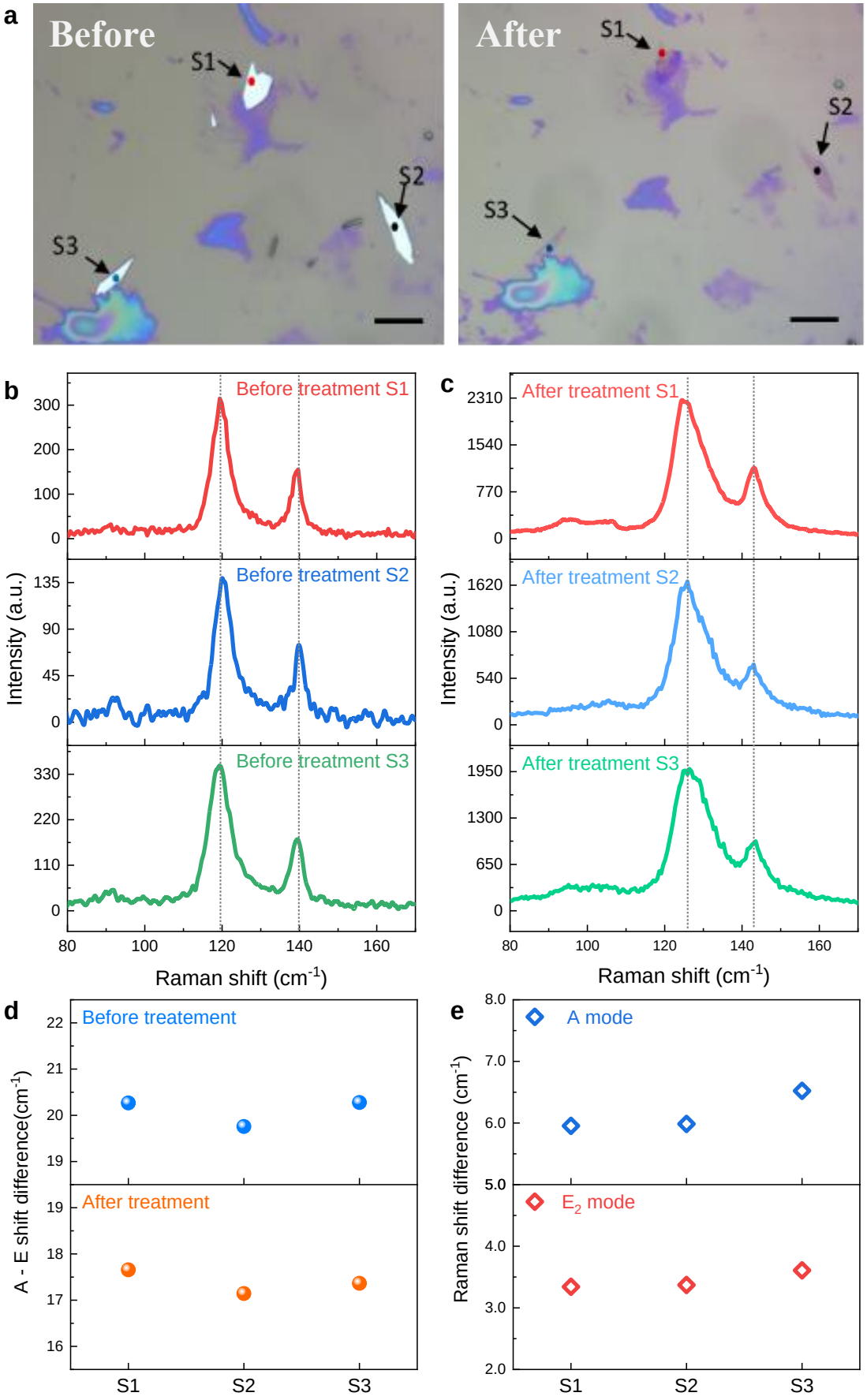
a
Before
S1
S2
S3
After
S1
S2
S3
b
Before treatment S1
Before treatment S2
Before treatment S3
Intensity (a.u.)
Raman shift (cm-1)
c
After treatment S1
After treatment S2
After treatment S3
Intensity (a.u.)
Raman shift (cm-1)
d
Before treatement
After treatment
A - E shift difference(cm-1)
S1
S2
S3
e
A mode
E2 mode
Raman shift difference (cm-1)
S1
S2
S3

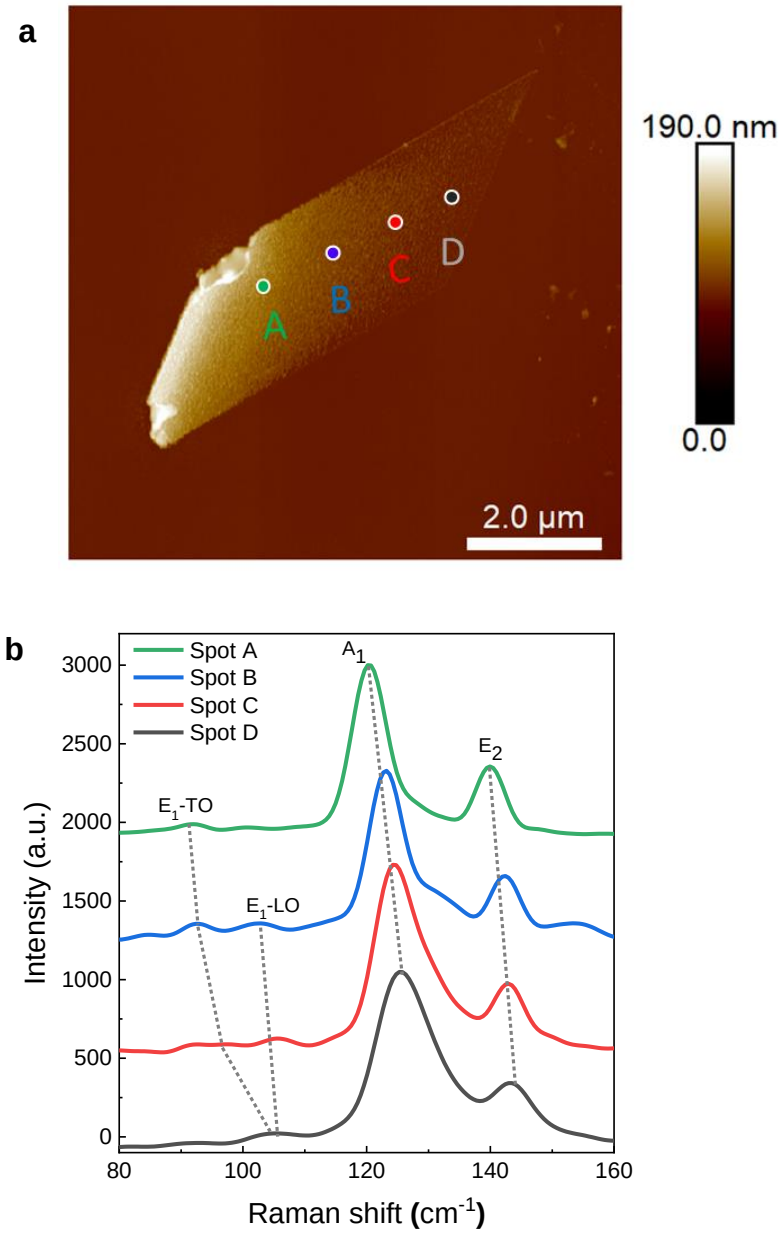

Supplementary Figure 7 | Location-dependent Raman measurements of the processed tellurene flake with the inclined surface. (a) AFM image of the processed tellurene flake with inclined plane geometry. **(b)** Raman spectra extracted from the locations highlighted in (a), where the corresponding Raman spectra exhibited clear blue shifts of all three peaks, and split and merge transition in E_1 mode when the test sites move from location A to D.

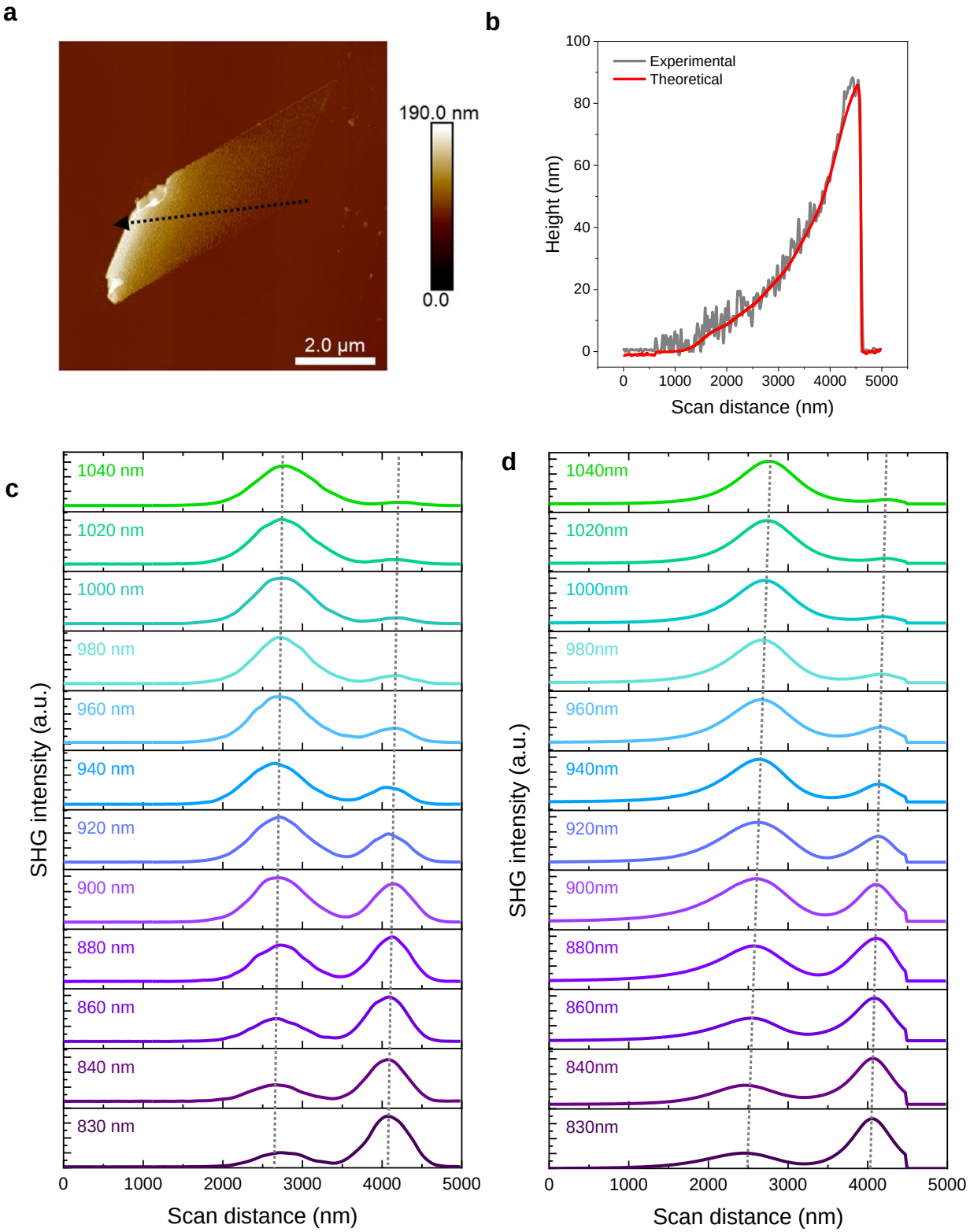

Supplementary Figure 8 | The experimental and theoretical SHG intensity profiles of treated inclined flakes under varying excitation wavelength. (a) AFM image of an

incline surface tellurene flake after plasma treatment. **(b)** Experimental height profiles (grey) extracted along white dashed lines in (a), and the theoretical height profile (red) governed by the mean thickness of experimental one, which have a good agreement. **(c)** The experimental SHG intensity profile extracted along the dash line in Fig 4b, with excitation wavelength ranging from 820nm to 1040nm, where the local largest emission sites get closer moderately under shorter wavelength excitation. **(d)** Analytical SHG profiles at corresponding wavelengths based on the mean height values of treated surface in (b), where the locations of local largest emission sites are remarkably influenced by the excitation of shorter wavelength, suggesting that the SHG emission of the smooth-surfaced flake is primarily reliant on the optical cavity effect rather than the pump light absorption.

Reference List

1. Martin, R. M.; Lucovsky, G.; Helliwell, K., Intermolecular bonding and lattice dynamics of Se and Te. *Physical Review B* **1976,** *13* (4), 1383-1395.

2. Wang, Y.; Qiu, G.; Wang, R.; Huang, S.; Wang, Q.; Liu, Y.; Du, Y.; Goddard, W. A.; Kim, M. J.; Xu, X.; Ye, P. D.; Wu, W., Field-effect transistors made from solution-grown two-dimensional tellurene. *Nature Electronics* **2018,** *1* (4), 228-236.

3. Wang, X.; Jones, A. M.; Seyler, K. L.; Tran, V.; Jia, Y.; Zhao, H.; Wang, H.; Yang, L.; Xu, X.; Xia, F., Highly anisotropic and robust excitons in monolayer black phosphorus. *Nature Nanotechnology* **2015,** *10* (6), 517-521.

4. Pine, A. S.; Dresselhaus, G., Raman Spectra and Lattice Dynamics of Tellurium. *Physical Review B* **1971,** *4* (2), 356-371.

5. Rao, G.; Fang, H.; Zhou, T.; Zhao, C.; Shang, N.; Huang, J.; Liu, Y.; Du, X.; Li, P.; Jian, X.; Ma, L.; Wang, J.; Liu, K.; Wu, J.; Wang, X.; Xiong, J., Robust Piezoelectricity with Spontaneous Polarization in Monolayer Tellurene and Multilayer Tellurium Film at Room Temperature for Reliable Memory. *Adv Mater* **2022,** *34* (35), e2204697.

6. Yang, D.-Q.; Zhu, L.-Q.; Wang, J.-L.; Xia, W.; Zhang, J.-Z.; Jiang, K.; Shang, L.-Y.; Li, Y.-W.; Hu, Z.-G., Band Structure and Lattice Vibration of Elemental Tellurium Investigated by Temperature-Dependent Mid-and-Far Infrared Transmission and Raman Spectroscopy. *physica status solidi (b)* **2022,** *259* (7).

7. Ling, X.; Huang, S.; Hasdeo, E. H.; Liang, L.; Parkin, W. M.; Tatsumi, Y.; Nugraha, A. R. T.; Puretzky, A. A.; Das, P. M.; Sumpter, B. G.; Geohegan, D. B.; Kong, J.; Saito, R.; Drndic, M.; Meunier, V.; Dresselhaus, M. S., Anisotropic Electron-Photon and Electron-Phonon Interactions in Black Phosphorus. *Nano Letters* **2016,** *16* (4), 2260-2267.

8. Wu, W.; Qiu, G.; Wang, Y.; Wang, R.; Ye, P., Tellurene: its physical properties, scalable nanomanufacturing, and device applications. *Chem Soc Rev* **2018,** *47* (19), 7203-7212.

9. Peng, M.; Xie, R.; Wang, Z.; Wang, P.; Wang, F.; Ge, H.; Wang, Y.; Zhong, F.; Wu, P.; Ye, J.; Li, Q.; Zhang, L.; Ge, X.; Ye, Y.; Lei, Y.; Jiang, W.; Hu, Z.; Wu, F.; Zhou, X.; Miao, J.; Wang, J.; Yan, H.; Shan, C.; Dai, J.; Chen, C.; Chen, X.; Lu, W.; Hu, W., Blackbody-sensitive room-temperature infrared photodetectors based on low-dimensional tellurium grown by chemical vapor deposition. *Science Advances* **2021,** *7* (16), eabf7358.

10. Wang, C.; Wang, P.; Chen, S.; Wen, W.; Xiong, W.; Liu, Z.; Liu, Y.; He, J.; Wang, Y., Anisotropic Properties of Tellurium Nanoflakes Probed by Polarized Raman and Transient Absorption Microscopy: Implications for Polarization-Sensitive Applications. *ACS Applied Nano Materials* **2022,** *5* (2), 1767-1774.

11. Yan, R.; Simpson, J. R.; Bertolazzi, S.; Brivio, J.; Watson, M.; Wu, X.; Kis, A.; Luo, T.; Hight Walker, A. R.; Xing, H. G., Thermal Conductivity of Monolayer Molybdenum Disulfide Obtained from Temperature-Dependent Raman Spectroscopy. *ACS Nano* **2014,** *8* (1), 986-993.

12. Su, L.; Zhang, Y.; Yu, Y.; Cao, L., Dependence of coupling of quasi 2-D MoS2 with substrates on substrate types, probed by temperature dependent Raman scattering. *Nanoscale* **2014,** *6* (9), 4920-7.

13. Anees, P.; Valsakumar, M. C.; Panigrahi, B. K., Temperature dependent phonon frequency shift and structural stability of free-standing graphene: a spectral energy density analysis. *2D Materials* **2015,** *2* (3), 035014.

14. Pawbake, A. S.; Erande, M. B.; Jadkar, S. R.; Late, D. J., Temperature dependent Raman spectroscopy of electrochemically exfoliated few layer black phosphorus nanosheets. *RSC Advances* **2016,** *6* (80), 76551-76555.

15. Zouboulis, E. S.; Grimsditch, M., Raman scattering in diamond up to 1900 K. *Physical Review B* **1991,** *43* (15), 12490-12493.

16. Gao, Z.; Tao, F.; Ren, J., Unusually low thermal conductivity of atomically thin 2D tellurium. *Nanoscale* **2018,** *10* (27), 12997-13003.

17. Yan, Z.; Jiang, C.; Pope, T. R.; Tsang, C. F.; Stickney, J. L.; Goli, P.; Renteria, J.; Salguero, T. T.; Balandin, A. A., Phonon and thermal properties of exfoliated TaSe2 thin films. *Journal of Applied Physics* **2013,** *114* (20).

18. Schinke, C.; Christian Peest, P.; Schmidt, J.; Brendel, R.; Bothe, K.; Vogt, M. R.; Kröger, I.; Winter, S.; Schirmacher, A.; Lim, S.; Nguyen, H. T.; MacDonald, D., Uncertainty analysis for the coefficient of band-to-band absorption of crystalline silicon. *AIP Advances* **2015,** *5* (6), 067168.

19. Cheng, M.; Wu, S.; Zhu, Z.-Z.; Guo, G.-Y., Large second-harmonic generation and linear electro-optic effect in trigonal selenium and tellurium. *Physical Review B* **2019,** *100* (3).

20. Szarvas, T.; Kis, Z., Numerical simulation of nonlinear second harmonic wave generation by the finite difference frequency domain method. *J. Opt. Soc. Am. B* **2018,** *35* (4), 731-740.